

8-2010

Targeting the Blood-brain Barrier with a Non-canonical Iron-mimicry Mechanism

Michael G. Ozawa

Follow this and additional works at: https://digitalcommons.library.tmc.edu/utgsbs_dissertations

Recommended Citation

Ozawa, Michael G., "Targeting the Blood-brain Barrier with a Non-canonical Iron-mimicry Mechanism" (2010). *The University of Texas MD Anderson Cancer Center UTHealth Graduate School of Biomedical Sciences Dissertations and Theses (Open Access)*. 58.
https://digitalcommons.library.tmc.edu/utgsbs_dissertations/58

This Dissertation (PhD) is brought to you for free and open access by the The University of Texas MD Anderson Cancer Center UTHealth Graduate School of Biomedical Sciences at DigitalCommons@TMC. It has been accepted for inclusion in The University of Texas MD Anderson Cancer Center UTHealth Graduate School of Biomedical Sciences Dissertations and Theses (Open Access) by an authorized administrator of DigitalCommons@TMC. For more information, please contact digitalcommons@library.tmc.edu.

Targeting the Blood-brain Barrier with a Non-canonical Iron-mimicry Mechanism

by

Michael G. Ozawa, B.S.

APPROVED:

Wadih Arap, M.D., Ph.D.
Supervisory Professor

Russell R. Broaddus, M.D., Ph.D.

Frederick F. Lang, M.D.

Renata Pasqualini, Ph.D.

Richard L. Sidman, M.D.

APPROVED:

Dean, The University of Texas
Health Science Center at Houston
Graduate School of Biomedical Sciences

Targeting the Blood-brain Barrier with a Non-canonical Iron-mimicry Mechanism

A

DISSERTATION

Presented to the Faculty of
The University of Texas
Health Science Center at Houston
and
The University of Texas
M. D. Anderson Cancer Center
Graduate School of Biomedical Sciences
in Partial Fulfillment

of the Requirements

for the Degree of

DOCTOR OF PHILOSOPHY

by

Michael G. Ozawa, B.S.
Houston, Texas

August 2010

DEDICATION

To all of the individuals and families that have been afflicted with cancer, your passion and strength has been an inspiration.

ACKNOWLEDGEMENTS

To begin, I would like to extend my deepest gratitude to Drs. Wadih Arap and Renata Pasqualini. Together, they run a world-class research program that remains a fun, collegial and rewarding work environment. Throughout my studies, their encouraging and supportive mentorship has helped me mature as a scientist and an individual. I have them both to thank for helping bring my academic career to this point, culminating in this dissertation, and for projecting a positive and successful outlook for my future.

This project was a highly collaborative effort engaging a large number of eager and committed collaborators from multiple institutions including The University of Texas M. D. Anderson Cancer Center, Texas A&M University, the Ludwig Institute for Cancer Research, the Center for Molecular Imaging Research at Massachusetts General Hospital, and Harvard Medical School. This work would certainly not have been possible without your time, effort, and assistance.

To all of the members of my committees, I am extremely thankful for your insightful questions, constructive criticisms, and encouraging comments. Every meeting has helped me develop my analytical skills and to convey this work in a clear and concise manner.

To all of the past and present members of the Arap/Pasqualini laboratory, your friendship and constant support has been priceless. To Fernanda Staquicini, this project would not be where it is without your leadership and guidance. To Marina Cardó-Vila, thank you for your constant willingness to help and listen over the years. To Magda Barbu, despite a short tenure with you, your knowledge and skills have been invaluable. To Wouter Driessen, I am thankful for your friendship and our ability to meet any deadline. And, lastly, to Dawn Christianson, thank you for your friendship and helping keep me on track.

To my family and friends, I wish to thank all of you for every interaction and conversation we have had, as they have made me who I am and have helped me fulfill my potential. Finally, most importantly, I would like to give a special and much-deserved thanks to my wife, Tara George, and daughter, Leighton Ozawa. Your encouragement and understanding have helped keep me grounded and have been a guiding force during my graduate work. I am humbled to have you both in my life and would not have made it through a single day or the past few years without your unwavering support and compassion. You are both my inspiration, and I will be indebted to you both always. Thank you.

Targeting the Blood-brain Barrier with a Non-canonical Iron-mimicry Mechanism

Publication No. _____

Michael G. Ozawa, B.S.

Supervisory Professor: Wadih Arap, M.D., Ph.D.

Treatment of central nervous system (CNS) diseases is limited by the blood-brain barrier (BBB), a selective vascular interface restricting passage of most molecules from blood into brain. Specific transport systems have evolved allowing circulating polar molecules to cross the BBB and gain access to the brain parenchyma. However, to date, few ligands exploiting such systems have proven clinically viable in the setting of CNS diseases.

We reasoned that combinatorial phage-display screenings *in vivo* would yield peptides capable of crossing the BBB and allow for the development of ligand-directed targeting strategies of the brain. Here we show the identification of a peptide mediating systemic targeting to the normal brain and to an orthotopic human glioma model. We demonstrate that this peptide functionally mimics iron through an allosteric mechanism and that a non-canonical association of (i) transferrin, (ii) the iron-mimic ligand motif, and (iii) transferrin receptor mediates binding and transport of particles across the BBB. We also show that in orthotopic human glioma xenografts, a combination of transferrin receptor over-expression plus extended vascular permeability and ligand retention result in remarkable brain tumor targeting. Moreover, such tumor targeting attributes enables *Herpes simplex*

virus thymidine kinase-mediated gene therapy of intracranial tumors for molecular genetic imaging and suicide gene delivery with ganciclovir. Finally, we expand our data by analyzing a large panel of primary CNS tumors through comprehensive tissue microarrays. Together, our approach and results provide a translational avenue for the detection and treatment of brain tumors.

TABLE OF CONTENTS

Dedication.....	iii
Acknowledgements.....	iv
Abstract.....	vi
Table of Contents.....	viii
List of Figures.....	x
List of Tables	xii
List of Abbreviations.....	xiii
Chapter 1: Introduction and review of the literature.....	1
Chapter 1.1: The blood-brain barrier.....	4
Chapter 1.1.1: Transferrin and Transferrin Receptor.....	9
Chapter 1.2: Phage display.....	11
Chapter 1.2.1: AAVP.....	17
Chapter 2: Methods.....	21
Chapter 3: Results.....	36
Chapter 3.1: Receptor-mediated delivery of targeted phage particles across the intact BBB.....	36
Chapter 3.2: The targeting peptide CRTIGPSVC binds to Tf:TfR through an allosteric mechanism.....	44
Chapter 3.3: CRTIGPSVC-phage targets Tf:TfR <i>in vivo</i>	53
Chapter 3.4: Targeted transgene delivery and molecular imaging of brain tumors.....	67
Chapter 4: Discussion.....	77

Chapter 5: Summary and Significance..... 82

Chapter 6: References..... 83

Chapter 7: Vita.....100

LIST OF FIGURES

Figure 1.	Genetic alterations and disease progression in glioblastoma.....	2
Figure 2.	Transferrin receptor internalization and recycling pathway.....	12
Figure 3.	General filamentous phage display vector structure.....	13
Figure 4.	Sequence alignment of phage clones recovered from <i>in vivo</i> phage display screening.....	37
Figure 5.	Peptide cluster mapping of transferrin.....	38
Figure 6.	Targeting specificity of phage displaying the peptide CRTIGPSVC in normal mouse brain.....	40
Figure 7.	Homing of CRTIGPSVC-phage and insertless phage to non-CNS control organs.....	41
Figure 8.	Pharmacokinetic study of targeted and insertless phage.....	42
Figure 9.	Brain microvessel depletion confirms blood-brain barrier transport.....	43
Figure 10.	CRTIGPSVC-phage interacts with apo-transferrin.....	45
Figure 11.	CRTIGPSVC-phage binds to apo-transferrin.....	46
Figure 12.	Removal of iron from holo-transferrin by EDTA.....	48
Figure 13.	<i>In vitro</i> phage binding assay to apo- and holo-transferrin in the presence of free iron.....	50
Figure 14.	EDTA-mediated chelation abolishes phage binding to apo-transferrin.....	51
Figure 15.	CRTIGSPVC peptide-induced conformational change assessed by steady-state fluorescence analysis.....	52
Figure 16.	CRTIGSPVC peptide-induced conformational change assessed by circular dichroism analysis.....	54

Figure 17.	Expression of transferrin receptor in normal brain and human glioblastoma xenograft.....	57
Figure 18.	CRTIGPSVC-phage targets orthotopic brain tumors.....	58
Figure 19.	Homing of CRTIGPSVC-phage and insertless phage to non-CNS control organs.....	59
Figure 20.	Pharmacokinetic study of blood half-life for CRTIGPSVC and insertless phage in tumor bearing mice.....	61
Figure 21.	CRTIGPSVC-phage targets subcutaneous brain tumor xenografts.....	62
Figure 22.	CRTIGPSVC-phage targets human glioblastoma <i>in vivo</i>	64
Figure 23.	CRTIGPSVC-phage localizes to tumor blood vessels.....	65
Figure 24.	CRTIGPSVC-phage co-localizes with transferrin receptor in tumors.....	66
Figure 25.	Targeted therapy of an orthotopic model of human-derived glioblastoma xenograft.....	68
Figure 26.	Histopathologic analysis of brain tumors following targeted therapy.....	69
Figure 27.	Targeted molecular-genetic imaging of intracranial brain tumors.....	71
Figure 28.	Tumor apoptosis by CRTIGPSVC-AAVP therapy.....	72
Figure 29.	Transferrin receptor expression in comprehensive human glioma tissue microarrays.....	74
Figure 30.	Transferrin receptor is highly expressed in glioblastoma.....	75
Figure 31.	Transferrin receptor is expressed in primary human CNS tumors.....	76

LIST OF TABLES

Table 1.	Expression of receptor-mediated transporters in GBM	
	compared to normal brain.....	55

LIST OF ABBREVIATIONS

AAV	Adeno-associated virus
AAVP	AAV-phage
BBB	Blood-brain barrier
BLAST	Basic Local Alignment Search Tool
BSA	Bovine serum albumin
CD	Circular dichroism
CNS	Central nervous system
CT	Computed tomography
CVO	Circumventricular organs
DAB	3,3'-diaminobenzidine
DMEM	Dulbecco's modified eagle's medium
DFO	Desferroxamine
EDTA	Ethylenediaminetetraacetic acid
FBS	Fetal bovine serum
GBM	Glioblastoma
GCV	Ganciclovir
HSVtk	<i>Herpes simplex virus</i> thymidine kinase
LB	Luria-Bertani
MRI	Magnetic resonance imaging
O/N	Overnight
OD	Optical density
PBS	Phosphate buffered saline

PCR	Polymerase chain reaction
PEG	Polyethylene glycol
PET	Positron emission tomography
PFA	Paraformaldehyde
PI	Protease inhibitors
RT	Room temperature
TBS	Tris buffered saline
Tf	Transferrin
TfR	Transferrin receptor
TMA	Tissue microarray
TNF α	Tumor necrosis factor alpha
TU	Transducing units
VEGF	Vascular endothelial growth factor

CHAPTER 1: INTRODUCTION AND REVIEW OF THE LITERATURE

Malignant gliomas are the most common primary brain tumor in adults (1). In the United States, nearly 15,000 individuals will be diagnosed with malignant glioma annually (1). The incidence has remained relatively constant over the last decade; however, improvements in the sensitivity of diagnostic imaging techniques have lead to a slight increase in incidence in certain populations, including the elderly. While representing a relatively small percentage of total cancer diagnoses (~1% of all new cases diagnosed annually in the United States), malignant gliomas--comprising anaplastic astrocytomas and glioblastomas-- account for a disproportionately high number of deaths from central nervous system (CNS) related diseases (1).

To date, only ionizing radiation has been documented as a risk factor (2). Additional causal agents have been suggested, but are as of yet inconclusive, including head injuries, exposure to electromagnetic fields, or contact with N-Nitroso-N-methylurea containing compounds (2). A small percentage of patients will present with a family history of gliomas (~5%), often without an identified genetic link. Familial gliomas have also been linked to certain genetic conditions including Li-Fraumeni syndrome, resulting from germline mutations in p53, and Turcot's syndrome, resulting from mutations in mismatch repair genes.

Gliomas are classified according to the World Health Organization scale, grades I to IV, largely based on histological, genetic, and prognostic characteristics (summarized in **Fig. 1**) (3-5). The lowest grade gliomas, grade I pilocytic astrocytomas, are considered benign and potentially curable with surgical resection. Grade II gliomas, diffuse astrocytomas, are slow progressing lesions that are often incurable due to wide-spread infiltration early in the course

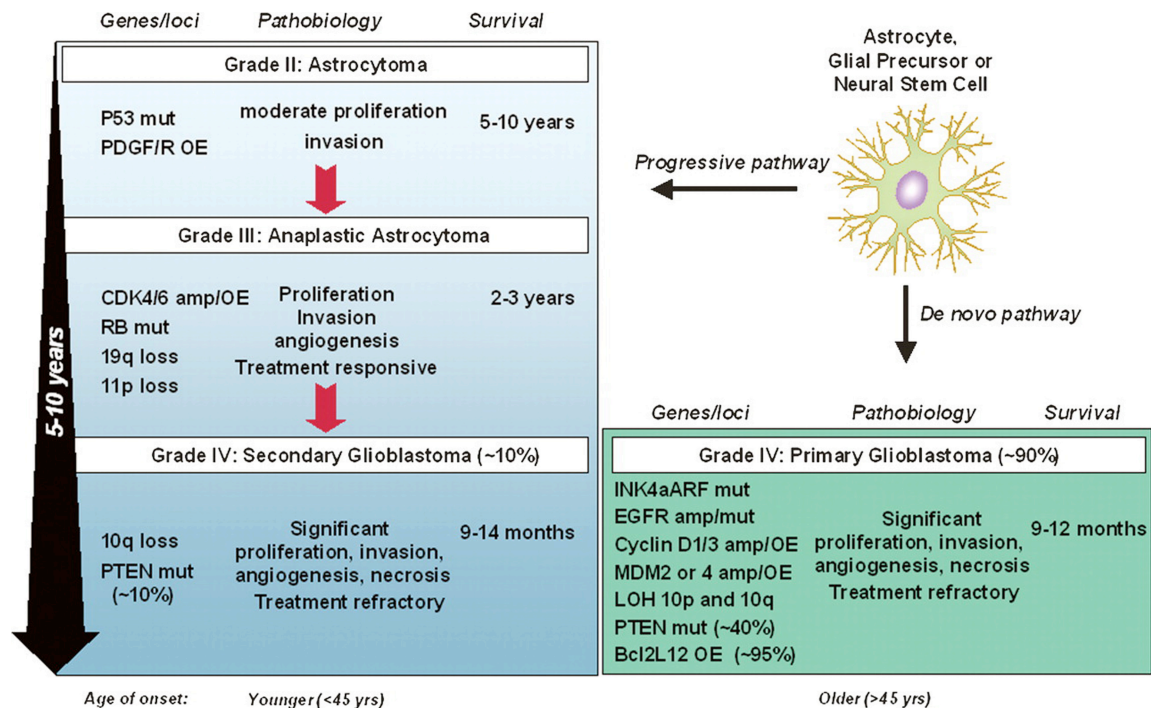


Figure 1. Genetic alterations and disease progression in glioblastoma. The scheme depicts the general epidemiology of glioblastoma, and the corresponding molecular and genetic aberrations associated with disease initiation and progression. Reprinted with permission, Furnari, F.B. et al., *Genes Dev* 21:2683-2710 (Reference 3), Copyright © 2007, Cold Spring Harbor Laboratory Press.

of the disease. With increased anaplasia and cellular proliferation, grade III gliomas or anaplastic astrocytomas, are often more aggressive and more rapidly lethal. Glioblastoma (GBM), grade IV glioma, is the most aggressive, invasive, and highest grade glioma marked by vascular proliferation or necrosis (pseudopallisading). GBM is responsible for nearly 60% of newly diagnosed gliomas and is often separated into two subtypes based on differences in molecular, genetic and clinical presentation: (i) primary and (ii) secondary (1). Primary glioblastomas often occur in patients at 50 years of age or older and are commonly characterized by amplifications in the epidermal growth factor receptor (EGFR) or deletions in phosphatase and tensin homologue on chromosome 10 (PTEN) and/or p16. Secondary glioblastomas arise from lower grade gliomas, including grade III anaplastic astrocytomas, present in patients less than 45 years old, and often overexpress platelet derived growth factor receptor (PDGFR), have mutations in p53, or alterations to the p16 or retinoblastoma (Rb) signaling pathways (3, 6).

Clinically, patients present with varied symptoms, including progressive headaches, seizures, and/or neurological alterations or defects. A diagnosis of glioblastoma is generally suggested by contrast-enhancing lesions from contrast-enhanced magnetic resonance imaging (MRI) or computed tomography (CT). However, definitive diagnosis of GBM predominantly remains a pathological assessment, often necessitating invasive tumor biopsies. GBM shares histological features with lower grade gliomas, including increased cellularity, nuclear atypia, and neoplastic astrocytes (5, 7). Yet, microvascular hyperproliferation or necrosis (including pseudopallisading) are often considered diagnostic features separating GBM from lower grade gliomas. Despite the known molecular and genetic differences between primary and secondary classifications, primary and secondary

GBM are pathologically indistinguishable and both respond similarly to standard therapeutic regimens. Of note, emerging genetic studies show promise in improving genetic stratifications and classifications (8, 9).

The standard of care for newly diagnosed GBM is maximal surgical resection combined with adjuvant radiotherapy and chemotherapy with temozolomide (10-12). Unfortunately, despite this aggressive therapeutic regimen, the median survival for patient remains 12-15 months and local recurrence is a leading cause of eventual mortality. Recent improvements in understanding the molecular and genetic characteristics of GBM have introduced several new classes of investigational agents, including receptor tyrosine kinase inhibitors (i.e., Erlotinib and Cetuximab), small molecule inhibitors of intracellular signaling pathways (i.e., Tamoxifen and Sirolimus), and antiangiogenic therapies (i.e., Bevacizumab) (3, 10, 13). However, the practical use of such newer therapeutic strategies for the treatment of brain tumors is often hampered by ineffective delivery of agents into the brain. Complicated by the presence of the highly specialized blood-brain barrier (BBB) and variability in microvascular functions at the blood-tumor interface, systemically circulated agents potentially meet highly restrictive barriers. As a result, many current drugs treating CNS disorders are created as highly lipophilic agents, leading to increased systemic toxicity and a lowering of the therapeutic index (14, 15). A clear need exists for improved therapies for the management and treatment of GBM.

CHAPTER 1.1: THE BLOOD-BRAIN BARRIER

Paul Ehrlich first suggested the existence of the BBB through experiments evaluating the tissue distribution of dye following intravenous administration and the lack of uptake by the

brain (16). Edwin Goldmann subsequently confirmed this hypothesis through a series of experiments generating the concept of an impermeable barrier between the systemic circulation and the brain (17). Further study of this phenomenon identified the brain microvascular cells and corresponding intracellular junctions as the functional barrier limiting passage (18). The current concept of the BBB has been refined to support a complex yet coordinated functional unit, termed the neurovascular unit, comprised of brain endothelial cells, astrocytes, perivascular neurons, and pericytes (19-21). Moreover, it is now known that the BBB is highly regulated and selective, not impermeable, separating both the brain parenchyma and spinal cord from circulating blood to maintain CNS homeostasis. The BBB physically exists at the level of brain capillaries; however, certain regions of the brain have less strict or absent barrier function, defined as the circumventricular organs (CVOs) (22). The CVOs are closely apposed to the third and fourth ventricles and include the area postrema, neurohypophysis, pineal gland, subfornical organ and the median eminence. Acting as sensory or secretory organs, the CVOs utilize extracellular transport systems and the presence of fenestrated (pores) within the endothelial lining - allowing free passage between blood and brain - to monitor the composition of the blood or to secrete hormones into the systemic circulation. Similarly, capillaries supplying the choroid plexus, which secretes cerebrospinal fluid, are fenestrated. Yet, it is the presence of tight junctions between cells within the epithelium that creates a barrier separating the cerebrospinal fluid from the brain.

Development of the BBB begins during embryogenesis as angiogenic blood vessels invade the neuroectoderm and anastomose to form the early brain microcirculation (23). The timing and arrangement of angiogenic sprouting is precisely regulated by a number of

interactions between growth factors and cognate receptors, the most well-studied of which is vascular endothelial growth factor (VEGF) and the VEGF receptor. Studies have demonstrated that a lack of VEGF is embryonically lethal, and the localization and diffusion of VEGF dictates the spatial patterning of the vascular network in development (24). The premature vascular network is largely considered abnormal, with prominent structural irregularities, large caliber blood vessels, and endothelial cell fenestrae (25). Such features are thought to render the brain capillaries permeable to small molecules, although the extent to which the vasculature is leaky during fetal development remains controversial. The early microvascular system also displays molecular profiles differentiating it from the BBB in the adult. Indeed, the presence of the glucose transporter-1 (Glut-1), the Src family tyrosine kinase lyn, P-glycoprotein, and MECA 32 antigen have all proven to serve as early markers of the developing vascular network (26).

The process of blood vessel maturation, and “barriergenesis,” is gradual and induced by external stimuli (27). The putative candidate(s) cell types eliciting molecular changes in the endothelium, including astrocytes, pericytes, extracellular matrix, and even neural progenitor cells, reside in close proximity to the brain microvessels. Yet, the exact cell type and molecular mediators driving barrier formation remains to be determined. Due to their close positioning near capillaries, and the timecourse of cell migration and differentiation, astrocytes have been implicated as potential sources of inductive signals (28). However, as astrocytes are also present in CVOs, this lends support to the notion that while functionally necessary, they do not drive BBB establishment. Pericytes, or mural cells, are required for the maturation and stabilization of the microcirculation and are encapsulated by a shared basement membrane with endothelial cells (29). Long cellular processes remain in intimate

contact with the endothelium and have been functionally implicated in the regulation of blood flow, particularly in the cerebrum (30). During developmental angiogenesis, pericyte migration occurs before microvessel sprouting and guides developing neovessels. A number of molecules acting on the endothelium have been identified, including angiopoietin-1 and PDGF-BB (29, 31). These factors have been identified as crucial molecules in establishing endothelial cell-pericyte interactions and function; however, definitive determination of BBB induction remains elusive. Similarly, while adhesion molecules, including cadherins and integrins, maintain cell-cell and cell-matrix interactions to ensure proper cellular function, it remains an open question as to whether molecules such as N-cadherin or $\alpha v \beta 8$ contribute to induce BBB establishment.

Although each component of the neurovascular unit contributes to the function of the BBB, capillary endothelial cells and associated tight junctions largely regulate permeability from blood to the CNS (18). The endothelial lining forming the BBB is a single layer of cells bound by a complex junctional network including tight, adherens, and gap junctions; the contribution of gap junctions to the BBB remains controversial. Both tight junctions and adherens junctions are marked by specific arrangements of protein components and accessory intracellular adapter proteins linked to the actin cytoskeleton. These all contribute to a high electrical resistance and formation of a physical impermeable barrier (21). Under normal conditions, the BBB restricts passage of plasma constituents, including circulating polar molecules, unless specific transport systems present on the endothelium are used (32). The general classes of known transport mechanisms allowing transcellular passage of necessary macromolecules and nutrients into the brain include: (i) lipid-mediated transport of lipid-soluble small molecules with molecular weights less than 400 Da, (ii) carrier-

mediated transport, (iii) receptor-mediated transport, (iv) ion transport, and (v) absorptive endocytosis (21). A number of carrier-mediated transporters at the BBB have been identified, including the monocarboxylate transporter 1, L1 amino acid transporter, and CNT2 adenosine transporter. One of the most well studied carrier-mediated transport systems is GLUT1, a brain endothelial specific glucose transporter (33). GLUT1 expression is differentially regulated, with a greater number of receptors present at the abluminal membrane than facing the lumen, which support a functional regulation of glucose between the blood and brain. Moreover, mutations in GLUT1 lead to seizures in infancy, developmental delay, and potential microencephaly, a condition termed GLUT1 deficiency syndrome (33). Circulating molecules such as insulin, transferrin and neuropeptides are unable to use small molecule carrier systems and require cell surface receptor-mediated transport for transcellular movement. Receptor-mediated internalization and transcytosis are highly regulated, often with receptor turnover rates much slower than in other anatomical locations, and this may potentially act as a mechanism to limit passage into the brain (34). To maintain interstitial fluid balance and pH, the sodium pump, sodium-potassium-chloride cotransporter, and several exchange transporters exist to regulate ion concentrations between the blood and brain and also demonstrate differential expression on the endothelial membrane (35).

Disruption of the BBB occurs in a number of disease states, including inflammatory disorders and cancer, permitting unregulated passage from the blood into the brain (21). The resultant influx of proinflammatory molecules and immune cells exacerbates the BBB breakdown as well as induces a secondary immune response by the resident CNS microglia. One of the early steps in BBB disruption is an increase in vascular permeability

accompanied by loosening of interactions between endothelial cells, particularly at the level of the tight junctions (18). Overexpression of HIF-1 α and VEGF have been causally linked to BBB alterations, and it was recently shown that high levels of VEGF disrupts the BBB through downregulation of claudin-5 and occludin expression (36). Indeed, several components of tight and adherens junctions have been implicated as either lost or altered in BBB disruption, including claudin-5, occludin, ZO-1, VE-cadherin, and β -catenin (18). Ultimately, the unpredictable barrier function and vascular blood flow associated with BBB disruption presents a challenge towards delivery of agents to therapeutic levels. As such, the temporal dynamics and relative contribution of BBB disruption to disease progression particularly in cancer and its impact on drug delivery remains an active area of basic and clinical research.

CHAPTER 1.1.1: TRANSFERRIN AND TRANSFERRIN RECEPTOR

Iron is an essential multi-functional element, acting as an enzymatic cofactor in diverse physiological processes or as a coordinating compound in macromolecules. The levels of iron within the body are narrowly regulated, primarily at the process of iron uptake, as loss of iron is minimal under normal conditions (37). Iron exists in two forms, either in a ferrous (Fe^{2+}) or ferric (Fe^{3+}) state. Despite such critical involvement in normal cellular function, free iron, particularly ferric iron, can lead to accumulation of insoluble compounds or to the generation of hazardous free radicals. To circumvent the toxic potential of iron, mechanisms including circulating protein carriers and intracellular storage molecules have evolved to limit the levels of free iron. One such family of iron transport proteins, that includes transferrin and the multi-functional protein lactoferrin, binds ferric iron and

distributes it through the systemic circulation (38). In fact, the crucial role of transferrin in maintaining homeostasis is supported by clinical observations from individuals lacking transferrin who suffer from growth retardation, anemia, manifestations of iron overload, and increased risk of infection (39).

Transferrin (Tf) is a ~80kD monomeric glycoprotein secreted largely from the hepatocytes, and to a lesser extent by Sertoli cells, ependymal cells, oligodendroglia, and several cancer cells (39, 40). The single polypeptide is functionally split into two homologous halves, termed the C- and N-lobes, connected by a small linker sequence. Each lobe is sub-divided into two domain structures containing a cleft for iron ion binding. As such, the iron free Tf (apo-transferrin; apo-Tf) is capable of binding either a single iron molecule (monoferric Tf) or two iron molecules (holo-transferrin; holo-Tf) (41). Binding, and eventual release of iron, is largely influenced by several factors including micro-environmental pH and relative ionic concentrations. In serum, the concentration of Tf is very stable, and it has a half-life of ~8-10 days, which affords an estimated 100 cycles of iron transport into cells (42). Clinically, iron saturation is a diagnostic measure to assess iron levels in the body, and typically Tf levels of holo-Tf represent 10-30% of the circulating pool (40).

The transferrin receptor (CD71; TfR) is a cell surface, monomeric glycoprotein predominantly found as a disulfide linked homodimer (43-45). With a short, single-pass transmembrane domain and a large extracellular domain, absence of this essential type 2 transmembrane protein causes embryonic lethality due to impairments in red cell and neuronal development. TfR is expressed at low levels in virtually all normal cells and is highly expressed in actively dividing cells, including cancer cells (45). TfR is robustly

expressed on the endothelium in the brain and has been the subject of intense study as an intrinsic mechanism of blood-brain barrier transport (46, 47). Expression is regulated post-transcriptionally by iron regulatory proteins interacting with iron response elements in the 3' untranslated region of the TfR mRNA(48). In addition, another homologous family member of the transferrin receptor family, TfR2, was described with regulation and expression that greatly differs from TfR (49). The expression of TfR2 is controlled by the cell cycle and not regulated by iron levels, and it has a much narrower tissue distribution profile, almost exclusively expressed in hepatocytes (50).

Typically, dietary iron crosses the epithelial lining of the duodenum via the divalent metal transporter 1 (DMT1) and into the portal circulation via ferroportin (48). Once in the circulation, ferric iron is rapidly sequestered by Tf (apo-Tf) and transported to target cells. Two molecules of holo-Tf bind the TfR homodimer located in clathrin-coated pits, and the complex is internalized by receptor mediated endocytosis. The endocytosed vesicle is transported to the endosome where the low intra-vesicular pH results in a conformational change in Tf, releasing iron. Iron is transported out of the endosome by the DMT1 and TfR is recycled back to the cell surface to release the iron-free apo-Tf. The entire cellular uptake process is reviewed in **Figure 2**.

CHAPTER 1.2: PHAGE DISPLAY

George Smith first described phage display as a methodology to probe binding sites of isolated antibodies (51). This work demonstrated that filamentous bacteriophage (phage) particles could be engineered to express protein fusion fragments inserted into surface capsid proteins (**Fig. 3**) (52). Using a fragment of the endonuclease *EcoRI* as a proof-of-

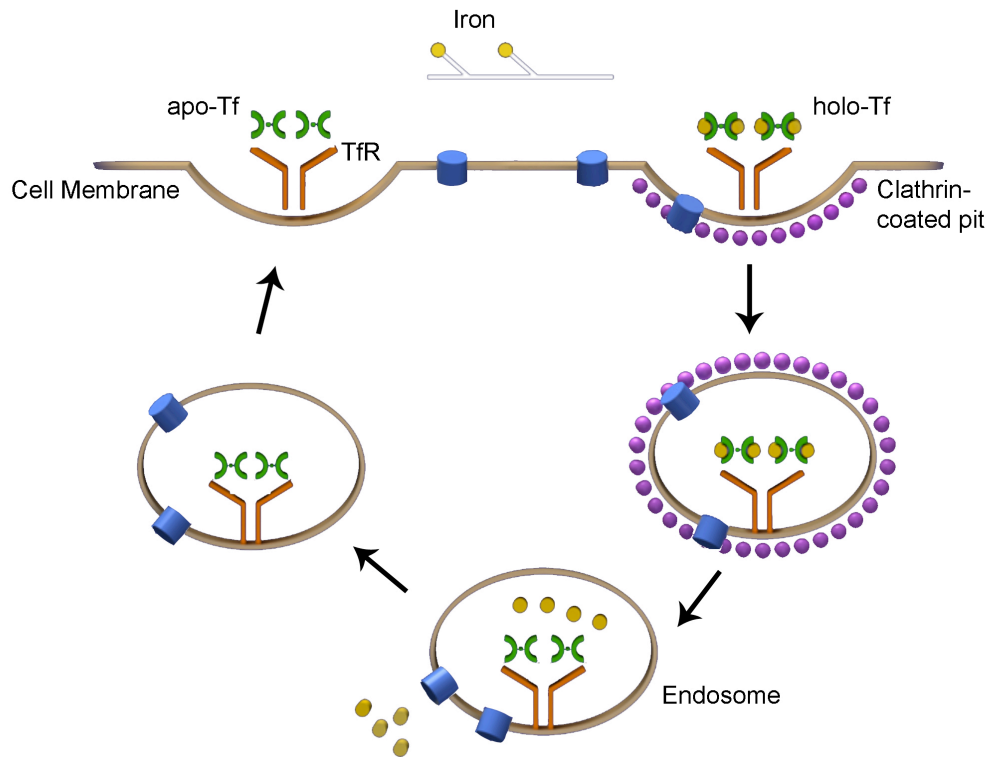


Figure 2. Transferrin receptor internalization and recycling pathway. Scheme depicts the typical receptor binding and cell internalization of iron-loaded transferrin. Image courtesy of Mr. David Bier.

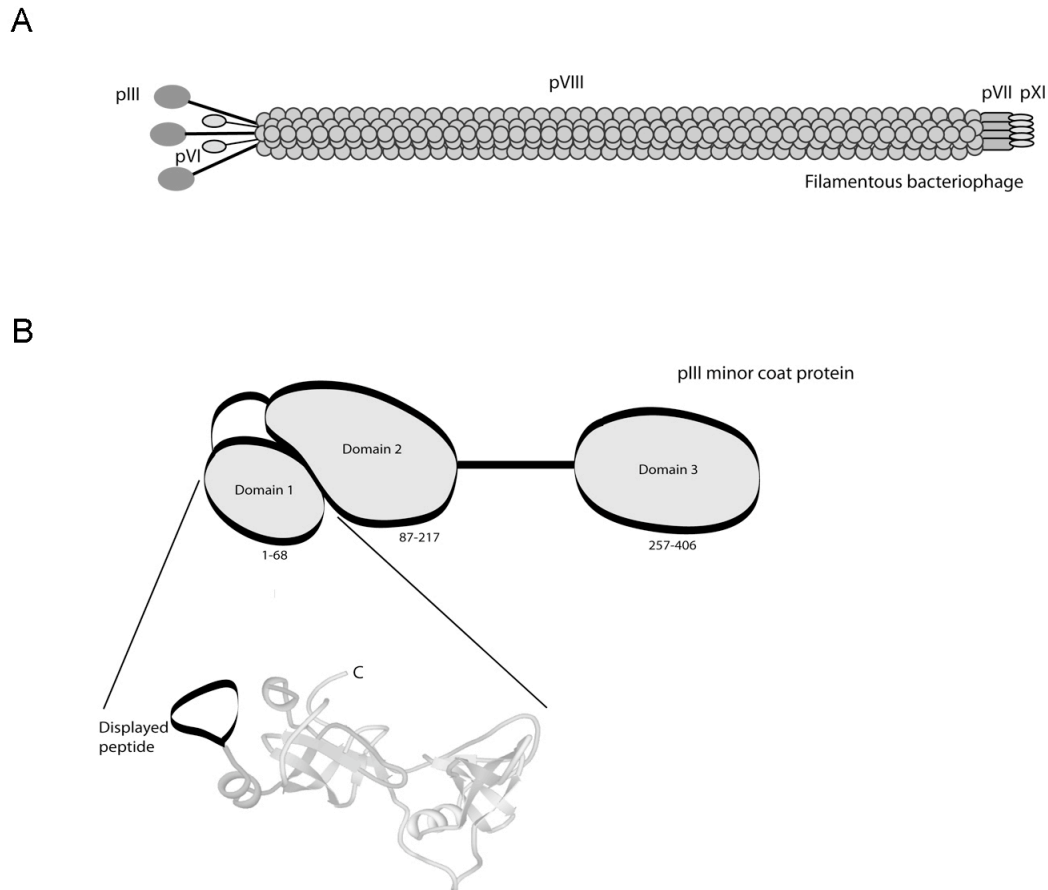


Figure 3. General filamentous phage display vector structure. (A) Diagram of the coat protein distribution for the pVIII major and pIII, pVI, pVII, and pXI minor coat proteins. (B) Scheme of pIII domain arrangement and location of pIII displayed peptides. Reprinted with permission, Ozawa, M.G. et al. In *CNS Cancer: Models, Markers, Prognostic factors, and Therapeutic approaches*. Ed. E.G. Van Meir (Reference 52). Copyright © 2009, Humana Press, New York.

concept, the resultant *EcoRI*-expressing phage remained biologically active, infecting host bacteria, while also binding to antibodies recognizing *EcoRI* (51). Sequential rounds of affinity selection confirmed binding specificity to the cognate antibody of *EcoRI*-displaying phage compared to wild-type phage. Subsequently, several independent groups expanded upon this initial work to generate libraries of phage clones displaying random peptide sequences. These combinatorial peptide libraries were then used as screening tools to identify residues mediating binding to antibody antigenic sites (53, 54). The method, termed “panning,” employed serial rounds of selection whereby phage adherence, recovery, and amplification permitted the identification of phage preferentially binding to a target. DNA sequence analysis of phage clones determined the amino acid sequence mediating binding, and in a larger context, the phage peptide sequences could then be compared through biochemical and bioinformatic-based assays to determine potential native proteins the phage sequence could functionally mimic. The approach has since been applied in the context of various diseases, such as cancer, as a means to identify cell surface antigens eliciting humoral responses in cancer patients. Indeed, Mintz *et al.*, through interrogation of circulating antibodies in a prostate cancer patient, identified glucose regulated protein-78 as a tumor antigen (55). Similarly, Vidal *et al.*, identified and characterized peptides mimicking heat shock protein 70 as being recognized by antibodies present in ascities fluid of ovarian cancer patients (56).

Through recognition of the diverse experimental conditions in which protein-protein interactions could be explored, a large number of groups expanded the technical and biological applications of phage display to settings *in vitro* and *in cellulo*. Screenings on isolated molecules have enabled identification of native protein ligands for receptors. For

example, phage display elucidated that the adhesion molecule beta-neurexin binds the *Staphylococcus aureus* microbial surface components recognizing adhesive matrix molecule (MSCRAMM) SdrC, and mapped key sites of interaction such as the tetratricopeptide repeat of the mitochondrial fission protein hFis1 (57, 58). Moreover, the identified peptides often have inherent activity, as studies have described active peptide inhibitors of trypsin isoenzymes and as well as growth factor receptor antagonists (59, 60). Similarly, profiling of cultured cells has afforded the opportunity to identify specific cell binding peptides in leukemia, molecular signatures for tumor types of the NCI-60 cancer cell panel, as well as differentially expressed receptors through comparative analysis of stimulated versus quiescent cells (61-63). These studies were enabled by a cell separation strategy coined biopanning and rapid analysis of serial interacting ligands, or BRASIL (61). In the proof-of-concept study, peptides specifically binding to VEGF stimulated endothelial cells were isolated and characterized following centrifugation through a density gradient. One peptide, CPQPRPLC, functionally mimicked VEGF and demonstrated binding specificity for both VEGFR-1 and Neuropilin-1. Subsequent studies identified the key residues mediating CPQPRPLC binding to VEGFRs and lead to the derivation of a small, retro-inverted peptide possessing anti-angiogenic properties (64, 65).

Concurrent to the rapid success of combinatorial phage display screenings *in vitro*, investigators explored the potential for identifying protein-protein interactions *in vivo*. The experimental approach in principle paralleled *in vitro* screenings, where a combinatorial library was intravenously administered and allowed to interact with the tissue of interest through the circulation; bound phage were recovered from tissues, amplified, and used for subsequent screenings to enrich for selective binding peptides. Pasqualini and Ruoslahti

pioneered the initial study *in vivo* demonstrating a unique distribution of peptides to the kidney and brain (66). In a subsequent study, phage display screenings on tumor xenografts were performed with the goal of identifying vascular markers of tumor endothelial cells. The tri-peptide motifs Arg-Gly-Asp (RGD) and Asn-Gly-Arg (NGR) were confirmed to mediate selective accumulation in tumors following systemic administration (67). Further characterization of the targeting motifs identified the cell surface receptor for RGD as the $\alpha v\beta 3$ and $\alpha v\beta 5$ integrins and the protease aminopeptidase N as the receptor for NGR. Moreover, the authors demonstrated that linking the motifs to chemotherapeutics resulted in robust reductions of tumor burden in pre-clinical tumor models. Thus, these data supported the emerging concept of vascular targeting as a novel paradigm to develop therapeutic or diagnostic agents that are more selective and efficacious.

More recently, to permit a more direct translation of identified targeting peptides to patients, several investigators have adapted phage display screenings to patients. In the first study in a human, Arap *et al.* administered a combinatorial phage display library to a terminal wean cancer patient and recovered several organ biopsies for analysis (68, 69). Focusing on the prostate, the group identified a peptide that bore primary sequence similarity to the human cytokine interleukin-11 (IL-11). Subsequent comparative study of the peptide, cognate protein, and native receptor revealed a new site of interaction on the exposed surface of IL-11 mediating binding to the IL-11 receptor alpha (IL-11R α) (70). Evaluation of the IL-11:IL-11R α signaling axis in human prostate cancer identified a positive correlation between IL-11R α expression and cancer progression and demonstrated that targeting of IL-11R α with a pro-apoptotic peptide yielded robust cellular apoptosis (71). These data led to the development of a novel, vascular-targeted, small molecule drug

candidate that is currently enrolling as a Phase I efficacy study. Supporting this patient-focused approach, Krag *et al.*, recently reported use of phage display libraries in a cohort of cancer patients (72). The authors performed serial screenings in the same patient and identified a non-random distribution of peptides to different tumor types. Taken together, future studies of phage distribution and identification of a human vascular map appears imminent.

CHAPTER 1.2.1: AAVP

Combinatorial phage display screenings, along with other genomic and proteomic methodologies, helped advance the identification of molecular differences between different cell and tissue compartments. Exploitation of such unique characteristics, including endothelial cell heterogeneity between organs, enabled strategies for site-specific delivery to diseased cells and vascular targeting through the systemic circulation. These concepts naturally garnered much enthusiasm to integrate targeting ligands to other systems for improved therapeutic indices. Indeed, one such area was the field of gene therapy, where one of the basic tenets is to deliver modifying genes specifically to diseased cells, thereby limiting untoward effects on normal cells. While the applications for gene delivery have greatly expanded beyond simple gene replacement strategies to include use of oncolytic viruses as local therapy (73), precise delivery to target cells remains most paramount (74). Thus, among the numerous critical factors and fundamental challenges for successful gene therapy approaches, delivery specificity, adequate cell transduction, and length of transgene expression remain the most elusive.

Mammalian viruses, such as adeno-associated virus (AAV), have an inherent tropism for all mammalian cells, high transduction efficiencies, and have been widely used in the field of gene therapy (75). However, this tropism is largely non-specific and previous attempts to enhance selective accumulation through manipulation of coat proteins resulted in overall lower transduction efficiencies (76). Thus, it stood to reason that systems that allow for ligand-directed targeting of vectors such as AAV could greatly improve cell transduction and efficacy of therapeutic regimens. Hajitou *et al.*, exploited the similarities between phage and recombinant AAV to generate a chimeric gene delivery vehicle that possessed specific genomic elements from both viruses, coined as AAV-Phage (AAVP) (77). This initial study reported that the chimera preserved the targeting properties afforded by phage-displayed peptides while also maintaining high *in vitro* and *in vivo* transduction rates from AAV. Moreover, this novel reagent readily integrated into the genome and formed transgene concatamers, which in combination allowed for prolonged gene expression for up to 50 days *in vitro*.

In vivo, AAVP particles engineered to target alpha v integrins readily accumulated in pre-clinical tumor models and allowed for delivery of various transgene cassettes, including GFP and *Herpes simplex virus* thymidine kinase (*HSVtk*); the latter acting both as a molecular-genetic imaging tool as well as a gene-directed enzyme prodrug therapy strategy (78, 79). The introduction of the *HSV* thymidine kinase into cells creates a system whereby nucleoside substrates are phosphorylated, preventing export out of the cell (80). When radiolabeled nucleosides are administered, such as the clinically applicable [¹⁸F]-FEAU, cells expressing *HSVtk* retain the radioactivity, and this allows for imaging by positron emission tomography (PET) and determination of tissue organ and localization. One week

after a single administration of targeted AAVP-*HSVtk* to tumor bearing animals, localization of [^{18}F]-FEAU demonstrated robust and dynamic transgene expression within the tumor (77). Serial evaluation over time within the same animal suggested that targeted AAVP-*HSVtk* allowed for monitoring of tumor cell growth and expansion dynamics. Similarly, HSVtk-mediated phosphorylation of the nucleoside analog ganciclovir (GCV), which is used clinically to treat cytomegalovirus infections, generates a pro-drug capable of genomic integration and eventual cellular apoptosis. Hajitou *et al.*, utilized this suicide-gene therapy approach with targeted AAVP-*HSVtk* and observed dramatic tumor mass reductions in both immunocompromised and immunocompetent animals. Corresponding PET imaging validated the net decrease in tumor volume through comparisons of pre- and post-treatment [^{18}F]-FDG, an indicator of metabolic activity and tumor viability, and [^{18}F]-FEAU levels.

As the prototype targeted AAVP-*HSVtk* predominantly localized to the tumor vasculature, it was proposed that vascular disruption and resultant hypoxia induced tumor cell apoptosis and tumor growth suppression. However, given the robust therapeutic efficacy, it remained plausible that more than one molecular mechanism contributed to the overall effect. Subsequent studies of alpha v integrin-targeted AAVP-*HSVtk* *in vivo* revealed that (i) endothelial cells highly expressing alpha v integrins were readily transduced by the AAVP vector, (ii) tumor cells with low integrin expression had very low transduction rates, and (iii) apoptosis following GCV therapy occurred in tumor and endothelial cells (81). Mechanistically, AAVP was shown to elicit a heterotypic bystander effect, as endothelial cells transduced with *HSVtk* were sufficient to induce apoptosis in both endothelial and adjacent, non-transduced tumor cells. Intercellular gap junctions, with connexins 43 and 26 playing a critical role, mediated transmission of *HSVtk* therapy.

Ultimately, this heterotypic effect combined with the vascular disruption, among other as yet unrecognized mechanisms, contributed to targeted AAVP-*HSVtk* therapeutic efficacy.

In support of this initial work, use of targeted AAVP hybrid vectors has expanded through generation of vectors carrying additional transgenes and application to other tumor models. For example, investigators recently developed an endothelial cell-targeted AAVP vector delivering tumor necrosis factor alpha (TNF α) (82). While the biological activity of TNF α is suggested to be concentration dependent, at high local levels it can function both as an anti-tumor and anti-angiogenesis agent. Thus, specific delivery and generation of TNF α within tumors could produce a dramatic anti-tumor effect. Administration of the targeted AAVP-TNF α demonstrated selective delivery to the vascular compartment within the tumors and mediated significant tumor reduction compared to controls. More recently, the targeted AAVP-TNF α was applied in the first pre-clinical trial of the Comparative Oncology Trials Consortium sponsored by the National Cancer Institute (83). The resultant data successfully identified dose ranges and generated pre-clinical support for potential translation to a Phase I study. Thus, the aggregate of these initial studies with AAVP suggest that targeted delivery of transgenes, including the dual-functioning *HSVtk* gene, is highly efficacious and may lead to clinically applicable therapeutic and diagnostic tools.

CHAPTER 2: METHODS

Reagents. The following primary antibodies were used: goat polyclonal anti-TfR (R&D Systems); mouse monoclonal anti-TfR (Fisher Scientific); rabbit polyclonal anti-bacteriophage (Sigma), rat monoclonal anti-CD31 (BD Pharmingen), and rabbit polyclonal anti-CD31 (AbCam). Secondary HRP-conjugated anti-rabbit IgG, Cy3-conjugated anti-rabbit IgG, Cy5-conjugated anti-hamster IgG, and FITC-conjugated anti-rat IgG were purchased from Jackson ImmunoResearch Laboratories. Human TfR (> 95% purity) and FragELTM were purchased from Calbiochem, and human apo-Tf (> 90% purity) and holo-Tf (> 90% purity) from R&D Systems. All synthetic peptides were synthesized and cyclized according to our specifications by commercial vendors (AnaSpec or PolyPeptide Laboratories).

Cell culture. U87-MG human glioblastoma cells (ATCC) were maintained in Dulbecco's modified Eagle's medium (DMEM) containing 10% fetal bovine serum (FBS), penicillin (100 units/ml), streptomycin (100 µg/ml), and L-glutamine (2 mM) (84). Rat gliosarcoma cells (9L) were obtained from ATCC and rat gliosarcoma cells expressing human TfR (9L 3.9) were obtained as described (85). Cells were maintained in DMEM supplemented with 10% FBS and the selection drug geneticin (G418; Gibco).

Animals. Eight-week-old female nude (nu/nu) mice and Balb/c mice were housed in the animal facilities of the University of Texas M. D. Anderson Cancer Center (UTMDACC) in Houston, Texas or the Ludwig Institute for Cancer Research at the University of California

San Diego (LICR/UCSD) in La Jolla, California. All animal procedures were reviewed and approved by the Institutional Animal Care and Use Committees of these institutions.

Orthotopic human glioblastoma xenografts. We used a guide-screw system (86) to implant human glioma cells directly into the mouse brain. In brief, a customized guide screw (~2.6 mm long) containing a central channel (~0.5 mm in diameter) was inserted through the skulls of female nude mice at a location immediately above the caudate nucleus (~2.5 mm lateral, 1 mm anterior to the bregma). This site is widely used as a reliable location for intracranial orthotopic tumor xenografts. Mice were kept under deep anesthesia throughout the procedure. One week after implantation of the guide-screw, animals were re-anesthetized, and a solution of 5×10^5 human glioma cells in 5 μ L phosphate buffered saline (PBS; pH 7.4) was injected into the brain with a Hamilton syringe. The cell suspension was administered slowly (5 to 10 min) with the aid of an infusion pump (Harvard Apparatus). Following disbursement of the tumor cells, the needle was slowly removed to limit volume loss and a stylet was inserted into the screw to close the system and prevent cell leakage. Animal body temperature was maintained until full recovery from anesthesia. *In vivo* homing experiments with targeted and control phage were performed ~12-15 days after tumor implantation.

Subcutaneous human glioblastoma xenografts. Subcutaneous xenografts were established following subcutaneous injection of a cell suspension containing 3×10^6 U87-MG cells into the right flank of nude mice. Tumor homing experiments were performed when palpable subcutaneous tumor xenografts reached 6-8 mm in diameter.

Phage display selection and phage homing *in vivo*. *In vivo* phage display screening on the brain was performed as described (66, 87-89). In brief, a combinatorial phage library displaying short cyclic peptides (CX₇C; C, cysteine; X, any amino acid) was intravenously administered into anesthetized Balb/c mice via the tail vein. Animals received 10¹⁰ transducing units (TU) of the phage library diluted in 200 µl DMEM, and brains were collected after 24 h of systemic circulation. Brains were transferred to 1 ml DMEM containing a protease inhibitor cocktail (DMEM-PI; 1 mM 4-(2-Aminoethyl) benzenesulfonyl fluoride hydrochloride [AEBSF], 20 µg/ml aprotinin, 10 µg/µl leupeptin, 1 mM phenylmethylsulfonyl fluoride [PMSF]) and homogenized in a Dounce glass tissue grinder. The homogenate was vortexed for 30 sec and centrifuged at 4,000 rpm for 3 min, followed by removal of the supernatant. This wash step was repeated three times, and after the third wash, the pellet was incubated with 1.5 ml of host bacteria (*Escherichia coli*; K91kan^R) with an Optical Density at 600 nm (O.D.₆₀₀) of 2.0 for one hour at room temperature (RT). The admixture was diluted in 10 ml of Luria-Bretani (LB) media containing tetracycline (20 µg/ml) and kanamycin (100 µg/ml) for a further 20 min at RT. The solution was then plated in multiple aliquots on LB agar plates containing tetracycline (40 µg/ml) and kanamycin (100 µg/ml) and incubated at 37°C overnight (O/N). The following day, colonies were (i) counted to determine phage recovery and (ii) picked, separately amplified, and pooled for a successive round of screening. Three serial rounds of *in vivo* selection were performed.

For homing of selected phage *in vivo*, mice were deeply anesthetized and received 10¹⁰ TU of targeted phage or insertless control phage intravenously via the tail vein. After 10

min, 30 min, 6 h, or 24 h, mice were systemically perfused through the heart with 10 mL DMEM. Brain and control organs were collected and were (i) immersed in PBS for DNA extraction, (ii) fixed in 10% neutral buffered formalin (24 h fixation) or (iii) fixed in PBS containing 1% paraformaldehyde (PFA; 1 h fixation), followed by O/N incubation in a PBS solution containing 30% sucrose at 4°C.

Phage amplification, purification and titration. The amplification, purification, and titration of phage clones have been well described (87, 90). In brief, individual phage clones were incubated with host *E. coli* bacteria (K91kan^R; O.D.₆₀₀ = 2.0) for 30 min. The admixture was transferred to 500 ml LB containing tetracycline (40 µg/ml) and kanamycin (100 µg/ml) then incubated at 37°C for 16-18 h with agitation (250 rpm). The cultures were centrifuged for 15 min at 6,000 rpm and then the phage was precipitated from the supernatant by addition of 15% PEG/NaCl and incubation on ice for 4 h. Cultures were centrifuged for 30 min at 10,000 rpm, and the supernatant was discarded. The phage pellet was resuspended in 500 µl PBS and transferred to an eppendorf tube. The mixture was centrifuged at max xg in a tabletop centrifuge to remove residual bacterial contaminants then transferred to a new tube. Quantification of phage particles was accomplished by serial dilution of the each phage in PBS followed by infection with host *E. coli* bacteria. The mixtures were incubated for 30 min followed by duplicate plating of the admixture on LB agar plates containing tetracycline (40 µg/ml) and kanamycin (100 µg/ml). Plates were incubated at 37°C O/N and resultant colonies counted. Phage quantities were expressed as TU/µl.

Production and titration of phage-based expression vectors. Targeted AAVP chimeric vectors were engineered through two intermediate DNA constructs (78). First, we isolated plasmid DNA from overnight host bacterial cultures (*E. coli*; MC1061) for the fUSE5 and fMCS vectors using the QIAprep spin kit (Qiagen). Purified DNA was digested with *Bam*HI and *Sac*II (NEB) to generate compatible fragments of approximately 5.4kb (fUSE5) and 4.1kb (fMCS). The restriction products were precipitated, resuspended, and adjoined with the Rapid Ligation kit (Roche). This created a fUSE5-fMCS hybrid intermediate containing a targeting peptide insert (CRTIGPSVC or derivatives) and a multicloning site (MCS) for insertion of transgene cassettes.

To create the targeted AAVP carrying *HSVtk*, we first subcloned *HSVtk* into the pAAV-eGFP plasmid (enhanced GFP; Stratagene) to replace eGFP using the *Bam*HI and *Not*I restriction sites. The resultant pAAV-*HSVtk* plasmid was subsequently digested with *Pvu*II to produce a ~2.8 kb fragment containing *HSVtk* with functional inverted terminal repeats (ITRs). The *HSVtk* fragment was then ligated to a *Pvu*II digested, linearized, and dephosphorylated fUSE5-MCS plasmid with the Rapid Ligation kit (Roche). Correct orientation of the insert in each construct was verified by restriction and PCR analysis. AAVP vectors were isolated, purified, and titered similar to phage clones, described above.

Peptide sequence analysis. To identify motifs matching Tf among phage-displayed peptides homing to normal brain, an in-house Peptide Match software was codified in Perl 5.8.1 based on RELIC (91). The code is based on the standard Basic Local Alignment Search Tool (BLAST), and it scores the similarity between the selected peptides and protein from the N- to the C-termini by scanning overlapping motifs comprising each seven-mer

peptide in one-residue shifts and in both orientations (92). The peptide-protein similarity scores were calculated based on a BLOSUM62 amino acid substitution matrix, modified to adjust for rare amino acid representation. In order to discriminate significant similarity from non-specific background match, different similarity score thresholds were empirically set for selected peptides, based on their population sizes. Peptide matches are subsequently classified according to the BLOSUM62-defined numbers of peptide residues deemed “identical,” “highly similar,” or “similar” to the corresponding residue positions within the protein. Graphic mapping of peptide sequences along the protein was performed using a web-based software codified in Perl 5.8.1 and CGI. Maps of peptide/protein match hotspots were generated with R Project Version 2.2.1.

DNA and RNA isolation from tissue and quantitative real-time PCR. Total DNA was isolated from either 25 mg of tissue, 10 µl of non-coagulated blood, or 1 mm coronal brain tissue sections using the DNeasy® Blood and Tissue Kit (Qiagen). DNA samples were quantified by absorbance measurements (A_{260}) and aliquots were stored at -80°C. The amount of phage present in each tissue sample was determined by quantitative PCR using the 7500 Fast Real-Time PCR System instrument (Applied Biosystems). In a final volume of 15 µl, each reaction contained 60 ng or 25 ng total DNA, 1x Power SYBR Green PCR Master Mix (Applied Biosystems), and oligonucleotide primers amplifying a portion of the Tet^R gene (3.75 picomoles) (93):

fUSE5F1: 5'-TGAGGTGGTATCGGCAATGA-3'

fUSE5R1: 5'-GGATGCTGTATTTAGGCCGTTT-3'

The following cycle program was used:

Step 1: 50°C, 2 min

Step 2: 95°C, 10 min

Step 3: 95°C, 15 sec

Step 4: 60°C, 1 min; Repeat steps 3-4 x40.

To validate amplification of the desired product, a dissociation curve analysis with an initial denaturation for 15 sec at 95°C followed by sequential temperature elevation from 60°C to 95°C to re-anneal the products was performed. For each experiment, standard curves were created through serial dilutions of precisely quantitated fUSE5 plasmid, ranging from 2.4×10^2 to 2.4×10^6 copies, and calculated by the system software (7500 Fast System SDS software, version 1.3.1.21, Applied Biosystems) through regression analysis of the PCR curve crossing points from the plasmid dilutions. The phage content within each DNA sample was extrapolated through comparison of the observed amplification threshold to the calculated standard curve. All amplifications and calculations were performed with an ABI7500 Fast system, and all data points, including the standard curve, were determined from triplicate reactions.

For gene expression studies, two sets of total RNA were independently isolated from brain microvessel and parenchyma fractions with the RNeasy Mini Kit (Qiagen). DNA synthesis was performed with SuperScript[®] III First-Strand Synthesis System (Invitrogen) according to the manufacturer's instructions. The following primer pairs were used:

slc2a1 (glut-1):

5' TTCTCTGTCGGCCTCTTTGT 3'

5'AGGCCAACAGGTTTCATCATC 3'

VE-cadherin:

5' TCATCAAACCCACGAAGTCC 3'

5'TGTTTTTGCCTGAAGTGCTG 3'

Occludin:

5' CCTACTCCTCCAATGGCAAA 3'

5' GGCACCAGAGGTGTTGACTT 3'

Isolation of brain blood vessels. Fractionation of brain blood vessels was performed as described (94, 95). Mice aged 3–5 weeks were deeply anesthetized and perfused through the heart with 10 mL of PBS. Craniotomy was performed and the meninges were removed with cotton swaps. Brains were removed and homogenized in a 1 mL Dounce tissue grinder in ice-cold DMEM-PI containing 0.2% BSA. The resulting homogenate was diluted to a final volume of 5 mL, transferred to the top of a 30% (wt/vol) dextran solution, and centrifuged for 25 min at 3,000 g at 4°C. The myelin layer and pellet containing blood vessels were carefully collected and washed twice in DMEM containing 0.2% BSA. The final fractions were resuspended in an adequate volume and used for DNA or RNA extraction (see above).

Colony counting assay. Determination of phage content in tissues following systemic circulation by bacterial infection has been previously described (87, 90). Organ samples (brain, muscle, pancreas, liver, lung, kidney, and spleen) were weighed and processed in triplicate. Tissues were placed in a Dounce glass tissue grinder containing DMEM-PI and 1% BSA (DMEM-PI/BSA), homogenized and transferred to a 2 ml eppendorf tube. Tissue samples were then washed three times with ice cold DMEM-PI/BSA, mixed with DMEM-PI, and vortexed for 30 sec after each wash. Samples were centrifuged at 4000 rpm for 3 min, and the supernatant discarded carefully. After the third wash, samples were briefly vortexed to re-suspend and warmed to 37°C before adding host *E. coli* bacteria (K91kan^R). We then incubated the admixture with 1.5 ml of host *E. coli* bacteria (O.D.₆₀₀ = 2.0) for one hour at RT. The mixtures were transferred to tubes containing 10 ml of LB containing tetracycline (20 µg/ml) and kanamycin (100 µg/ml) and incubated at RT for 20 minutes. Multiple aliquots were plated in triplicate on LB agar plates containing tetracycline (20 µg/ml) and kanamycin (100 µg/ml) and incubated at 37°C O/N. The following day, phage content (TU) per mg of tissue was determined by counting formed colonies.

In vitro phage binding assays. TfR, apo-Tf, holo-Tf, and BSA were coated in triplicate wells of a 96-well microtiter plate O/N at 4°C. Wells were washed twice with PBS, blocked with PBS containing 3% BSA for 1 h at RT, and incubated with 10⁹ TU of phage for 1-2 hr. Wells were washed extensively with PBS (~12 times), and bound phage were recovered by infection with 200 µL of host *E. coli* bacteria (K91kan^R; O.D.₆₀₀ = 2.0). The mixtures were transferred to LB containing tetracycline (20 µg/ml) and kanamycin (100 µg/ml) at RT for 20 min then plated in multiple aliquots on LB agar plates containing tetracycline (20 µg/ml)

and kanamycin (100 µg/ml). Plates were incubated at 37°C O/N and resultant colonies counted. To test phage binding inhibition by free iron, an initial solution of 10 mM iron (III) phosphate (Fe₃PO₄) (Sigma) in double-distilled water was used. Final concentrations of iron ranged from 0.01 mM to 0.5 mM, where indicated.

Phage binding assays on cells. Cell-phage binding assays were performed as described (61). In brief, cultured cells were washed with PBS, detached with 5 mM EDTA, and resuspended in DMEM containing 10% FBS. Cells were manually counted using a hemocytometer and resuspended in the appropriate volume. A total of 10⁶ cells were incubated with 10⁹ TU of phage for 2 h on ice in the presence of either apo- or holo-Tf (200 µg/mL) in 200 µL DMEM. The liquid cell suspension was added to a 400 µL Eppendorf tube containing an organic solution (dibutyl phthalate:cyclohexane, vol/vol, 9:1; ρ = 1.03 g/ml) and centrifuged at 10,000 g for 10 min. The tube was immediately snap frozen to isolate the pellet. The tube bottom was carefully cut into an Eppendorf tube and residual organic solvent liquid was removed. The phage-cell pellet was resuspended and incubated with 200 µl of host *E. coli* bacteria (K91kan^R; O.D.₆₀₀ = 2.0). Phage/bacteria admixture was plated in multiple aliquots on LB agar plates containing tetracycline (40 µg/ml) and kanamycin (100 µg/ml), incubated at 37°C O/N, and counted for TU determination (see above).

Removal of iron from holo-Tf by chelators. Ten mg of holo-Tf were dissolved in 1 mL PBS (O.D.₄₅₀ = 0.3), and 100 µL of this solution was transferred to Slide-A-Lyzer MINI Dialysis Units (Pierce). Samples were dialyzed in EDTA or DFO solutions. The final

concentrations of chelating agents ranged from 0.05 mM to 50 mM, with minimal alteration in the final volume after 24 h. Transfer reactions were measured spectrophotometrically with an O.D.₄₅₀.

Steady-state fluorescence spectroscopy. Steady-state tryptophan fluorescence spectra for apo-Tf were obtained on a Spectrofluorimeter LS 50B (Perkin-Elmer). Increasing molar ratios of Fe⁺³, the targeted peptide CRTIGPSVC, or control peptides (control peptide 1: CGLPYSSVC; control peptide 2: CSGIGSGGC; control peptide 3: CRFESSGGC and control peptide 4: CPQRGVTPC) were incubated O/N at RT with 2 μM apo-Tf in buffer containing 100 mM HEPES, 10 mM NH₄CO₃, pH 7.4. Samples were excited at 295 nm and emission scans were collected from 305 to 400 nm with an excitation slit of 2.5 nm and an emission slit of 6 nm. All spectra were corrected for background fluorescence by subtraction of the appropriate blanks.

Circular dichroism (CD). CD spectra for apo-Tf were recorded on a Jasco J720 spectropolarimeter (JASCO Europe) from 230 to 320 nm, with a bandwidth of 1 nm and integrated for 1 sec at 0.2 nm intervals. Samples were measured at RT using cuvettes with a 2-mm path length. Absorbance values of Fe⁺³ and peptide alone were subtracted from the results. Increasing concentrations of Fe⁺³, the targeted peptide CRTIGPSVC, or control peptides (control peptide 1: CGLPYSSVC; control peptide 2: CSGIGSGGC; control peptide 3: CRFESSGGC and control peptide 4: CPQRGVTPC) were titrated in 100 μM of apo-Tf in buffer containing 100 mM HEPES, 10 mM NH₄CO₃, pH 7.4. The data were expressed as mean residue ellipticity, [θ], in deg cm² / dmol, which was calculated from $[\theta] = (d \times s \times$

$M)/(c \times l)$, where d denotes observed ellipticity (the displacement in cm from the baseline), s sensitivity in mdeg/cm, M , the mean residue weight, c , protein concentration in mg/mL and l , cell path length. The concentrations of protein were kept at 8 mg/mL.

High-density tissue microarrays (TMA). The construction of the human glioma TMA was previously described (96). Briefly, tissue arrays were constructed with a manual tissue arrayer (Beecher Instruments) with tissue cores extracted from formalin-fixed, paraffin-embedded archival tissue blocks obtained from the brain tumor bank at UTMDACC. The TMA included primary human gliomas with all histologic subtypes and grades of diffuse gliomas as codified by the World Health Organization classification (4, 5), including glioblastoma multiforme (GBM), anaplastic astrocytoma (AA), anaplastic oligodendroglioma (AO), oligodendroglioma (O), anaplastic mixed oligoastrocytoma (AMOA), mixed oligoastrocytoma (MOA), gliosarcoma (GS), and low-grade diffuse astrocytoma (LGA). LGAs were not analyzed here because of their small sample size ($n=4$).

Immunohistochemistry. Immunohistochemistry on sections of formalin-fixed, paraffin-embedded mouse and human tissue was performed with a labeled streptavidin biotin (LSAB) + peroxidase kit (DAKO). Slides were deparaffinized and rehydrated with xylene and graded concentrations of alcohols, blocked for endogenous peroxidases, and treated in a microwave oven with an antigen retrieval solution (DAKO). Slides were blocked for non-specific protein binding and treated with one of the following primary antibodies: (i) polyclonal rabbit anti-bacteriophage antibody (1:500 dilution), (ii) polyclonal rabbit anti-CD31 antibody (1:50 dilution), or (iii) polyclonal goat anti-TfR (1:50 dilution). After 1 h,

slides were washed three times with 20 mM Tris-buffered saline (TBS) containing 0.1% Triton X-100. Slides were next incubated for 1 h at RT with a peroxidase-conjugated anti-rabbit secondary antibody. Slides were washed three times with TBS containing 0.1% Triton X-100 and were developed with the specific substrate 3,3'-diaminobenzidine (DAB). Immunohistochemistry on glioma tissue microarrays and glioma xenografts were performed on an automated immunohistochemical autostainer (Lab Vision Corp.). Stained TMAs were evaluated and scored by a pathologist. Detection of apoptosis in paraffin-embedded specimens was performed with the FragEL™ DNA Fragmentation Detection Kit (Calbiochem) according to the manufacturers instructions. Hematoxylin was used as a nuclear counterstain in all experiments.

Immunofluorescence. Fluorescence immunohistochemistry was performed on cryostat sections (60 – 80 µm thickness) from 1% PFA-fixed tissues. Slides were washed three times with PBS and once with PBS containing 0.3% Triton X-100 (PBST; 5 min per wash) followed by non-specific protein block for 1 h with 5% normal serum diluted in PBST. Tissue sections were incubated with one or more of the following primary antibodies diluted in PBST containing 1% appropriate normal serum at RT for 1 h: (i) monoclonal rat anti-CD31 (1:500 dilution), (ii) polyclonal rabbit anti-bacteriophage (1:5000 dilution), (iii) polyclonal goat anti-TfR (1:1000 dilution). Sections were rinsed three times and stained for 1 h with appropriate Cy3-conjugated and FITC-conjugated secondary antibodies. Slides were washed three times in PBST, fixed in 4% PFA for 2 min, and washed three times with PBS. Fluorescence images were captured on an IX70 inverted fluorescence microscope

(Olympus). Confocal images were acquired on a laser scanning confocal microscope (Zeiss). Image analysis was performed with the Zeiss LSM 3.2 software package.

Radiolabeled substrate synthesis and quantification. Radiolabeled [^{18}F]-FEAU was synthesized to radiochemical purity (> 99%) using 5-ethyluracil-2,5-bis-trimethylsilyl ether as the pyrimidine base for condensation with 1-bromo-2-deoxy-2-[^{18}F]fluoro-3,5-di-*O*-benzoyl- α -D-arabinofuranose (97, 98). For quantification of [^{18}F]-FEAU radioactivity, regions of interest were digitally drawn on images and the measured values converted from nCi/mm³ into percentage of injected dose per gram of tissue [%ID/g] (79, 80).

Targeted molecular-genetic imaging. Orthotopic brain tumor-bearing animals received a single dose (10^{11} TU iv per mouse) of CRTIGPSVC-AAVP-*HSVtk* or control ~7 d after tumor implantation. A combination of positron emission tomography (PET) and computed tomography (CT) scans following iv administration of the radiolabeled nucleoside analog [^{18}F]-FEAU were used to determine HSVtk expression. For individual PET images, a microPET R4 (Concorde Microsystems) equipped with a computer-controlled positioning bed in a 10.8-cm transaxial and 8-cm axial field of view with no septa and operating in 3D list mode was used. Combined PET/CT imaging was performed with an Inveon micro-PET/CT scanner (Siemens Preclinical Solution). Glioma-bearing mice were anesthetized (2% isoflurane in 98% oxygen), temperature maintained at 38°C with a heat lamp, and submitted for imaging 2 h following intravenous [^{18}F]-FEAU administration. The microCT imaging parameters were: x-ray voltage of 80kVp, anode current of 500 μA , and exposure time of 300-350 milliseconds for each of the 360 rotational steps. Images were

reconstructed by a two-dimensional ordered subsets expectation maximization (OSEM) algorithm. PET and CT image fusion and image analysis were performed with vendor software ASIPro version 5.2.4.0 (Siemens Preclinical Solution).

Targeted therapy. Glioma-bearing animals (n=10 animals/group) received a single dose (10^{11} TU iv per mouse) of CRTIGPSVC AAVP-*HSVtk* or control ~7 d after intracranial tumor implantation. Treatment with ganciclovir (GCV; 80 mg/kg/day, ip) was initiated 7 d after AAVP administration and continued for 5 d. Animals were monitored and euthanized at the first sign of intracranial tumor burden. Following the treatment protocol, animals were euthanized and tumor sizes measured. Tissues were placed in 10% neutral buffered formalin for histological and immunohistological analyses.

Statistics. Experimental data values are expressed as means \pm standard error of the mean (SEM) from at least triplicate experimental data sets. In most settings, test and control data were compared using a Student's *t* test or ANOVA, where appropriate, and p values less than 0.05 were considered significant.

CHAPTER 3: RESULTS

Chapter 3.1: Receptor-mediated delivery of targeted phage particles across the intact BBB.

To gain insight into the repertoire of cell surface receptors present on the brain endothelium and identify ligand-receptor systems for targeted delivery, we employed an *in vivo* phage display screening strategy using a library of random CX₇C peptides (C, cysteine; X, any residues) (62, 67, 68, 88, 99). The phage library was intravenously administered into normal mice (66) and allowed to circulate for endothelial cell internalization and transport across the intact BBB *in vivo*. Following 3 rounds of serial selection (panning), we recovered an enriched population of brain-homing phage. The brain-targeting phage pool was analyzed by a series of custom bioinformatics software packages (62, 68) to identify candidate motifs and to minimize or eliminate background for further evaluation (62, 68). We then applied a basic local alignment and search tool (BLAST) of selected sequences online to detail protein alignment and to identify peptides with high similarity. More than 30 non-redundant peptide sequences (~20% of the total) showed similarity to the iron-binding molecule transferrin (Tf). This sub-pool was used for further analysis and prioritization. Three main clusters of candidate Tf-like motifs were identified and enclosed within the N-lobe of Tf: Clusters #1 and #3 matched to two distinct segments of domain N1 (at the N- and C-termini), while Cluster #2 was centered within domain N2 (**Fig. 4**). Three-dimensional models of the iron-bound Tf N-lobe (**Fig. 5A**, residues 1 – 331) and iron-bound Tf complexed to TfR (**Fig. 5B**) positioned cluster 2 around the iron atom, within the Tf iron-binding cleft. Clusters #1 and #3 were located on the exposed surface of Tf (100). Given the sequence similarity to an exposed surface of Tf, we initially focused our functional analysis

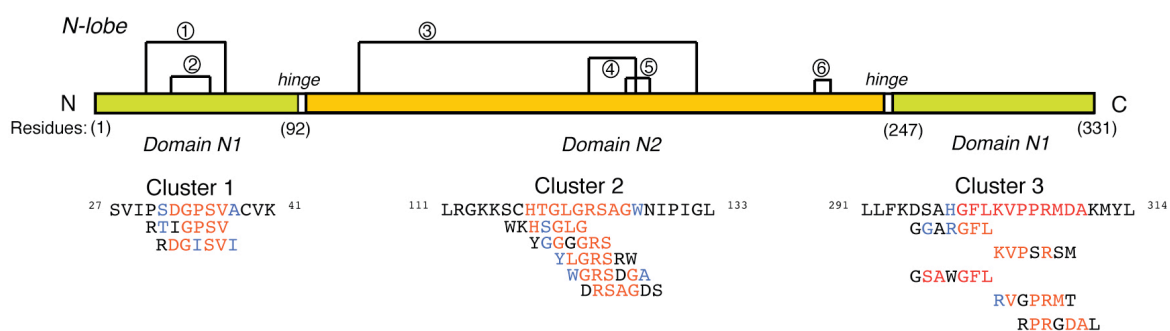


Figure 4. Sequence alignment of phage clones recovered from in vivo phage display screening. The scheme depicts the overall structure of the N-lobe half-molecule of transferrin. Domains N1 and N2 are indicated. The numbers represent the six consensus disulfide bonds: Cys10-Cys49, Cys20-Cys40, Cys119-Cys195, Cys159-Cys175, Cys162-Cys180, and Cys172-Cys178, respectively.

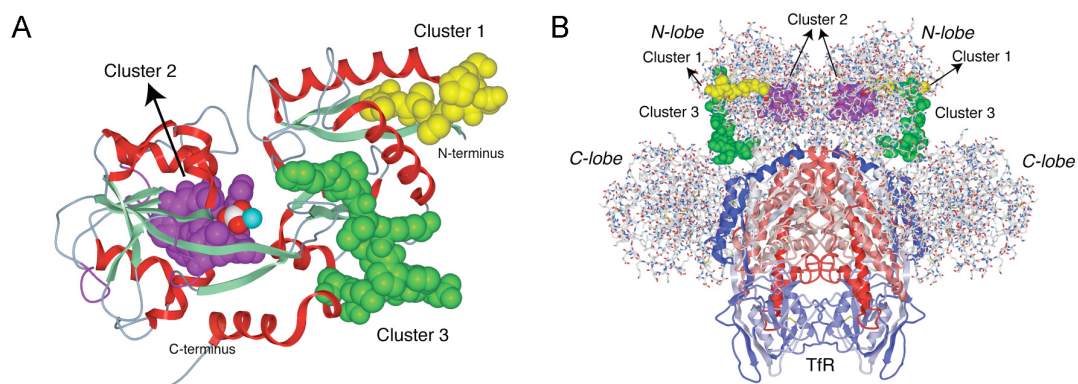


Figure 5. Peptide cluster mapping of transferrin. (A) Ribbon diagram showing the structural organization of iron-loaded transferrin and location of the peptide clusters. (B) Side-view of the transferrin:transferrin receptor molecular complex. N- and C-lobes are shown.

on the cyclic targeting peptide CRTIGPSVC, originally grouped in cluster 1. The remaining candidate peptides were not functionally pursued here.

To evaluate and confirm the targeting attributes of the selected peptide *in vivo*, we administered the CRTIGPSVC-phage intravenously into normal mice and first assessed homing by recovery from tissue homogenates, followed by counting of transducing units (TU) (not shown) and quantitative real-time PCR (**Fig. 6**). Non-targeted (insertless) phage and homing to non-CNS organs (shown is muscle) served as negative controls (**Figs. 6 and 7**). Phage was intravenously (iv) administered into tail veins of mice, and brains and control organs were surgically collected 10 min, 30 min, and 24 h later. Phage DNA was amplified by quantitative real-time PCR, and we detected ~100-fold more CRTIGPSVC-phage particles in the normal brain following a 10 min circulation compared to insertless phage (**Fig. 6**). A similar result was obtained at 30 min (**Fig. 6**), with a reduction to ~40-fold difference detected at 24 h post-administration (**Fig. 6**). Homing to skeletal muscle was at background levels for all timepoints. Next, to evaluate phage clearance and assess the contribution of phage degradation in targeting differences, we performed pre-clinical pharmacokinetic studies. We observed no significant differences in the half-lives of targeted and insertless phage in the blood of normal mice (**Fig. 8**) suggesting that superior uptake of targeted phage in the brain is mediated by specific ligand-receptor interactions and not an event of differential circulation. Lastly, brain microvessel separation from the brain parenchyma was used to confirm the ability of the CRTIGPSVC-phage to cross the intact BBB (**Fig. 9A**) (94, 95, 101). Normal mice were intravenously injected with targeted or insertless phage and brains were collected after 10 min, 30 min, and 24 h of systemic circulation. The tissue was homogenized and fractionated on a gradient of 30% dextran

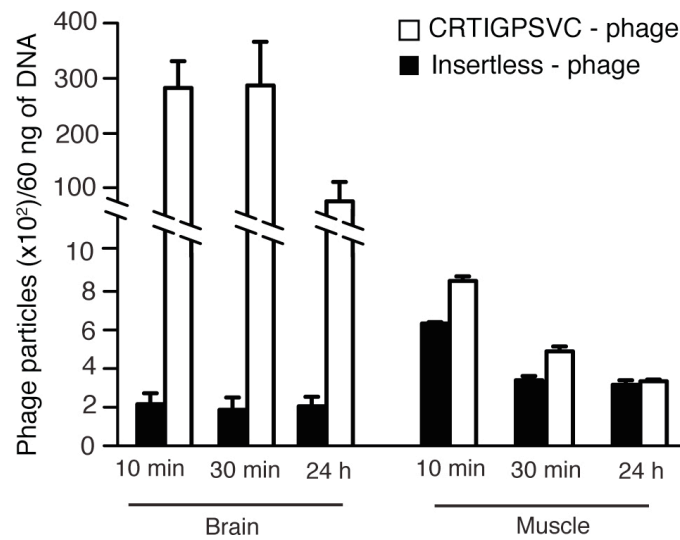


Figure 6. Targeting specificity of phage displaying the peptide CRTIGPSVC in normal mouse brain. The homing specificity of CRTIGPSVC-phage and insertless-phage in normal brain compared to non-brain control organ (shown is muscle). CRTIGPSVC-phage and insertless phage were administered intravenously into mice. Phage was allowed to circulate for 10 min, 30 min and 24 h, and tissues were recovered and processed as described.

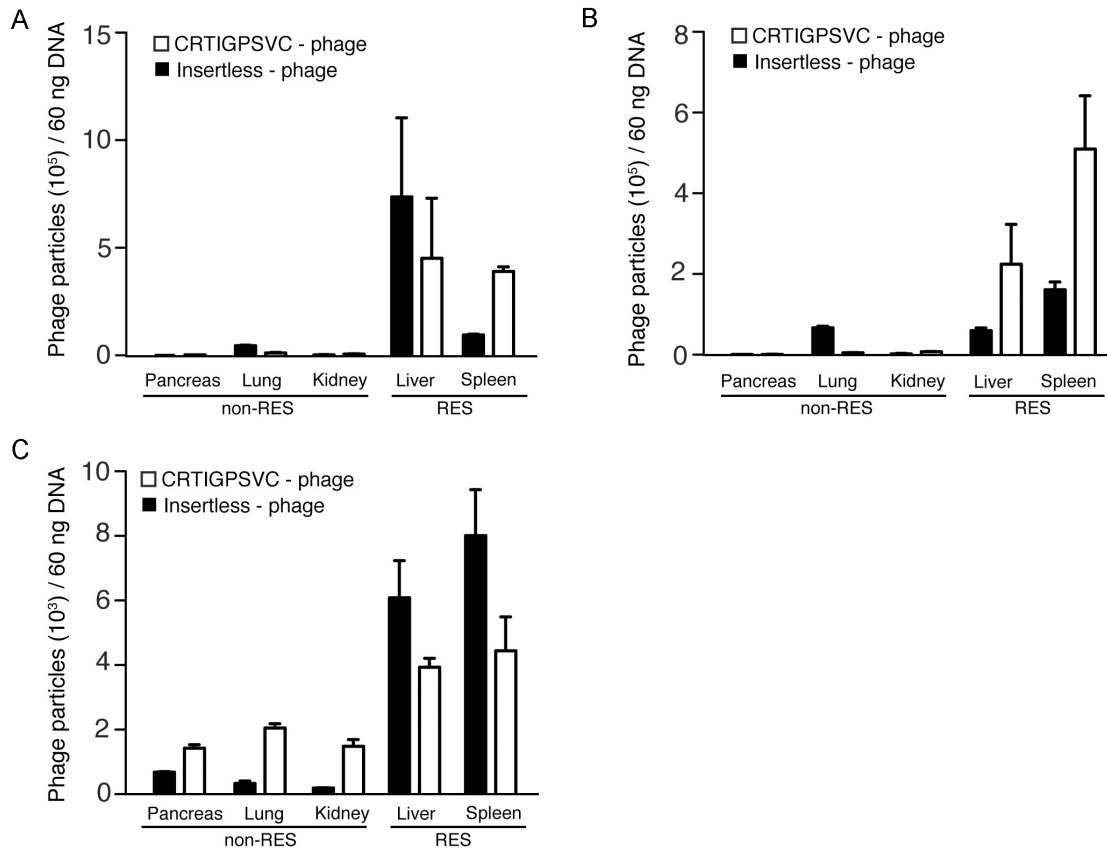


Figure 7. Homing of CRTIGPSVC-phage and insertless phage to non-CNS control organs. Mice were injected with 10^{10} TU of phage and organs were collected after 10 min (A), 30 min (B), and 24 h (C) of systemic circulation. Accumulation of phage particles is observed in the spleen and liver under all experimental conditions, a phenomenon caused by the non-specific clearance of phage within the reticulo-endothelial system (RES).

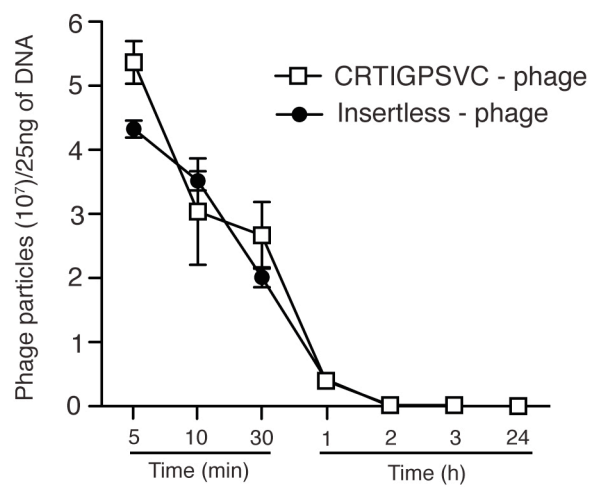


Figure 8. Pharmacokinetic study of targeted and insertless phage. CRTIGPSVC-phage and insertless phage were administered into normal mice and the half-life in blood was established. Data depict similar clearance irrespective of the presence of an insert peptide.

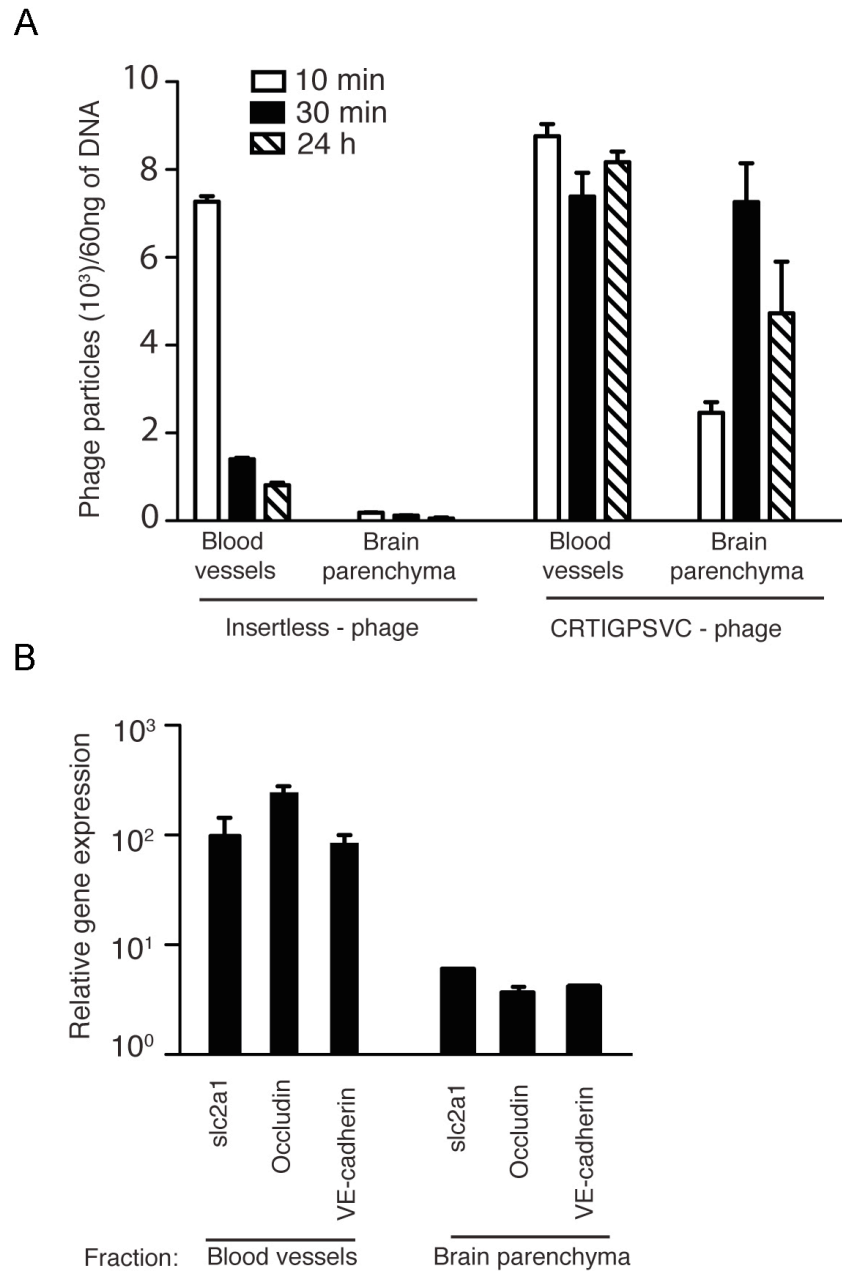


Figure 9. Brain microvessel depletion confirms blood-brain barrier transport. (A) Fractionation of brain microvessels and parenchyma confirmed the ability of the CRTIGPSVC-phage to cross the intact blood brain barrier. (B) Separation of microvessels from the brain parenchyma was confirmed by real-time quantitative PCR. Shown are markers of brain capillaries (slc2a1 and Occludin) and large blood vessels (VE-cadherin).

solution (wt/vol). Quantitative real-time PCR demonstrated the presence of CRTIGPSVC-phage in both fractions (blood vessels and blood vessel-depleted brain parenchyma). Insertless phage was not detected in the parenchyma fraction (**Fig. 9A**). We further used real-time PCR to confirm partial purity of the isolated fractions using genes specific for capillaries and endothelial cells (**Fig. 9B**).

Chapter 3.2: The targeting peptide CRTIGPSVC binds to Tf/TfR through an allosteric mechanism.

Having shown that targeted phage particles displaying the CRTIGPSVC peptide crossed the intact BBB, we next attempted to elucidate the molecular mechanism(s) mediating its transport from blood into normal brain. First, to establish whether CRTIGPSVC is a mimic of Tf, we evaluated the binding of CRTIGPSVC-phage to cells stably over-expressing human TfR and parental cells using a phage-based cell separation assay (**Fig. 10**) (61). To determine binding specificity, we tested the affects of apo-Tf (iron-free, open conformation) and holo-Tf (iron-containing, closed conformation) on the binding of phage to the cell surface. Unexpectedly, we observed enhanced binding when apo-Tf was added to the system (Student's *t* test, $p < 0.05$). This result indicated that CRTIGPSVC-phage interacts with apo-Tf resulting in enhanced binding to TfR. To more accurately determine CRTIGPSVC binding characteristics, we next analyzed the binding of CRTIGPSVC-phage to TfR, apo-Tf, and holo-Tf in a cell-free system. Insertless phage and BSA were used as negative controls. Consistently, we observed enhanced binding of CRTIGPSVC-phage to apo-Tf compared to TfR or holo-Tf (**Fig. 11**). As commercially available apo-Tf preparations often contain minute amounts of iron-loaded Tf contaminants

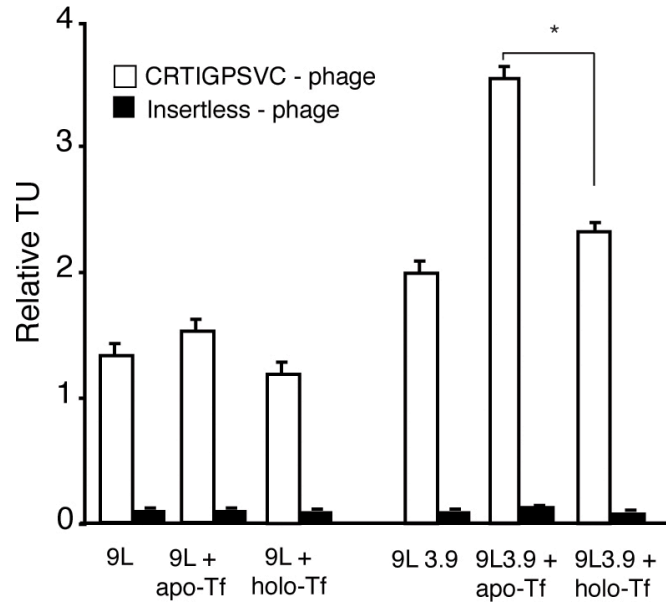


Figure 10. CRTIGPSVC-phage interacts with apo-transferrin. Binding of phage to rat gliosarcoma 9L cells and 9L cell expressing human transferrin receptor (9L3.9) in the presence of apo-transferrin and holo-transferrin. Statistically significant (*Student's *t* test, $p < 0.05$) binding to 9L3.9 in the presence of apo-Tf was observed with CRTIGPSVC-phage compared to holo-Tf.

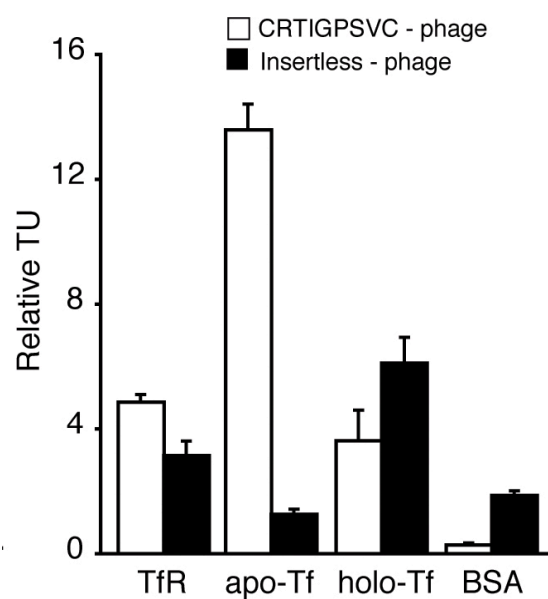


Figure 11. CRTIGPSVC-phage binds to apo-transferrin. Binding assays revealed that CRTIGPSVC-phage target apo-Tf in vitro. Insertless phage and BSA served as negative controls.

that could bias interpretation of our data, we used increasing concentrations of EDTA (from 0.05 mM to 50 mM) to remove iron from commercial holo-Tf and to generate an “iron-free apo-Tf preparation” (**Fig. 12A**). Desferroxamine (DFO), an effective free-iron-chelating agent that does not remove iron from holo-Tf, served as a negative control (102). We validated transfer of iron from holo-Tf to the chelating agents through spectrophotometric monitoring of changes in light absorption (**Fig. 12A**). Increasing amounts of EDTA linearly reduced light absorption, data indicating release of iron from holo-Tf (**Fig. 12A**); no changes in absorption were detected when holo-Tf was dialyzed against DFO under the same experimental conditions. Total removal of iron and change in protein conformation were achieved with 50 mM EDTA.

We next tested the binding of CRTIGPSVC-phage to the “iron-free apo-Tf”, in the presence of increasing concentrations of EDTA or DFO. As controls, we used apo- and holo-Tf. Phage displaying the peptide CRTIGPSVC bound only to the commercial apo-Tf preparation and to that obtained after dialysis of holo-Tf with 50 mM EDTA (**Fig. 12B**, arrows). As further confirmation of our previous results, we did not detect binding of CRTIGPSVC-phage to holo-Tf.

Given that CRTIGPSVC-phage binds selectively to apo-Tf, we hypothesized that the CRTIGPSVC peptide might functionally mimic iron. If so, it would stand to reason that binding of CRTIGPSVC, like binding of iron, would induce allosteric conformational changes in apo-Tf. This would allow for Tf binding to TfR, receptor dimerization, receptor endocytosis, and ultimately release of the peptide-targeted phage into the cytoplasm of TfR-positive cells. To test this hypothesis, we evaluated whether free iron and/or CRTIGPSVC synthetic peptide would compete with the binding of CRTIGPSVC-phage to apo-Tf. We

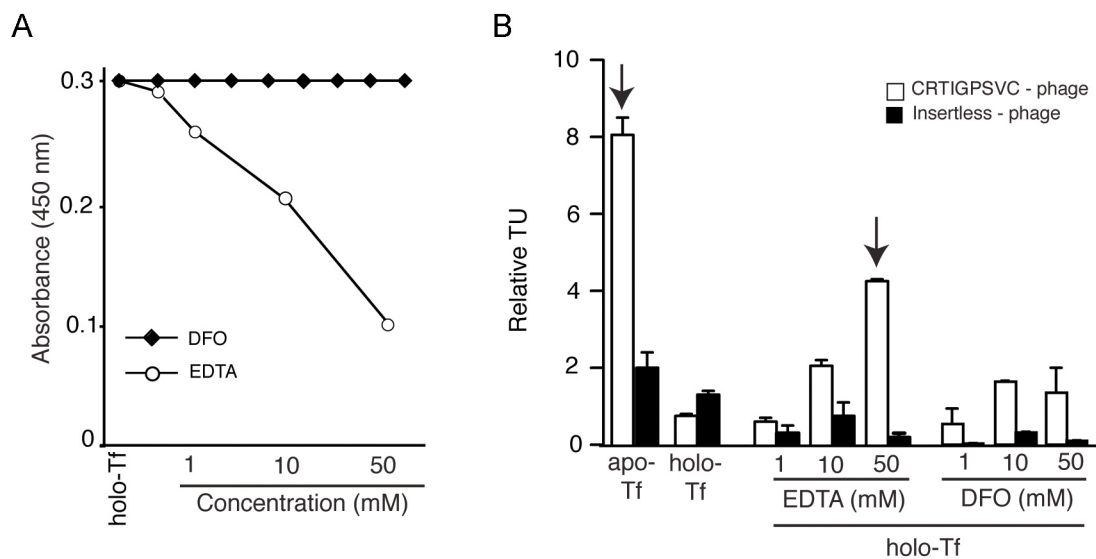


Figure 12. Removal of iron from holo-transferrin by EDTA. (A) The transfer reaction and removal of iron was measured spectrophotometrically at 450 nm. DFO was used as a control. (B) Phage binding assays to commercial apo-Tf and apo-Tf obtained after dialysis of holo-Tf with EDTA. The CRTIGPSVC-phage binds only to apo-Tf (arrows). No phage binding to holo-Tf was detected above background. Experiments were performed three times and a representative experiment is shown.

designed a series of phage binding assays *in vitro* to apo- and holo-Tf in the presence of several concentrations of ferric iron (Fe^{+3}), chelating agents, and CRTIGPSVC peptide (**Figs. 13 and 14**). We observed that iron at concentrations ranging from 0.01-0.5 mM abrogated binding of CRTIGPSVC-phage to apo-Tf (**Fig. 13A**) whereas no major alterations were observed in the binding of targeted phage to holo-Tf (**Fig. 13B**). Consistently, the effect of iron on the binding of peptide-targeted phage particles to apo-Tf or holo-Tf was reversed by the addition of EDTA (**Fig. 14**). *In vitro* phage binding assays revealed concentration-dependent iron chelation with EDTA, which reversed iron-induced binding inhibition of CRTIGPSVC-phage to apo-Tf (**Fig. 14A**). We noted no change in CRTIGPSVC-phage binding to holo-Tf in the same experimental setting (**Fig. 14B**). The same results were obtained with the CRTIGPSVC synthetic peptide, where increasing peptide concentrations abrogated binding of targeted phage to apo-Tf (data not shown). Together, these data suggest that CRTIGPSVC and iron have similar allosteric effects on apo-Tf, CRTIGPSVC binds to apo-Tf, and that CRTIGPSVC-phage functionally mimics iron. Moreover, these data are consistent with the hypothesis that selective internalization of the Tf:TfR:CRTIGPSVC complex into TfR-positive cells is mediated by conformational changes induced by CRTIGPSVC binding to apo-Tf.

To evaluate this working hypothesis, we applied optical methodologies, initially using analysis by steady-state fluorescence (**Fig. 15**) (103-106). First, we assigned changes in fluorescence spectra to apo-Tf in the absence or presence of Fe^{3+} (**Fig. 15A**). Next, we used increasing concentrations of the CRTIGPSVC peptide to evaluate changes in apo-Tf conformation as indicated by changes in fluorescence spectra; we observed a gradual shift of the apo-Tf fluorescence spectra in the presence of increasing amounts of the CRTIGPSVC

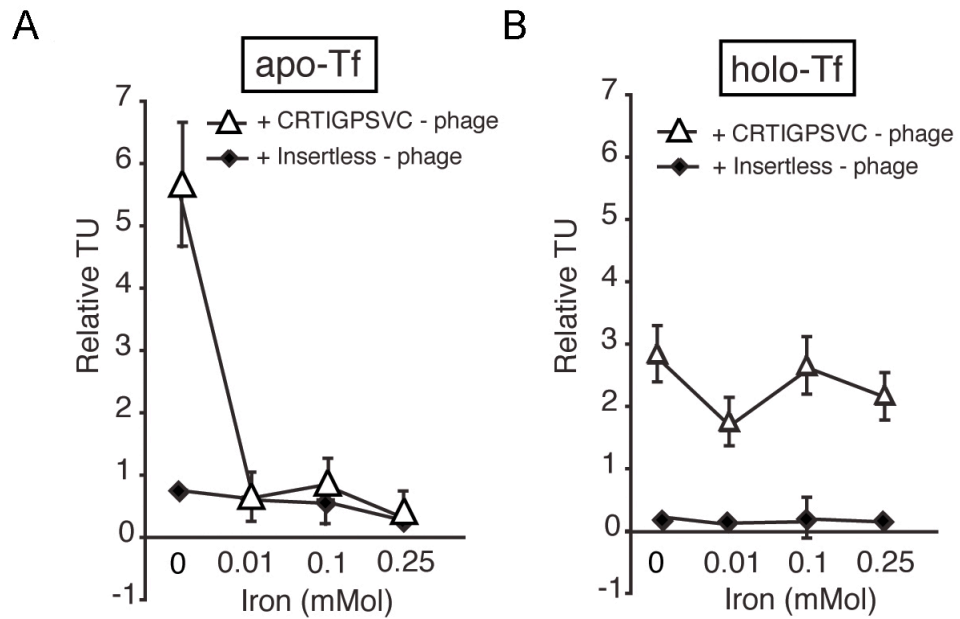


Figure 13. In vitro phage binding assay to apo- and holo-transferrin in the presence of free iron. (A) Iron inhibits the binding of CRTIGPSVC-phage to apo-transferrin in a concentration-dependent manner, but not its binding to holo-transferrin (B).

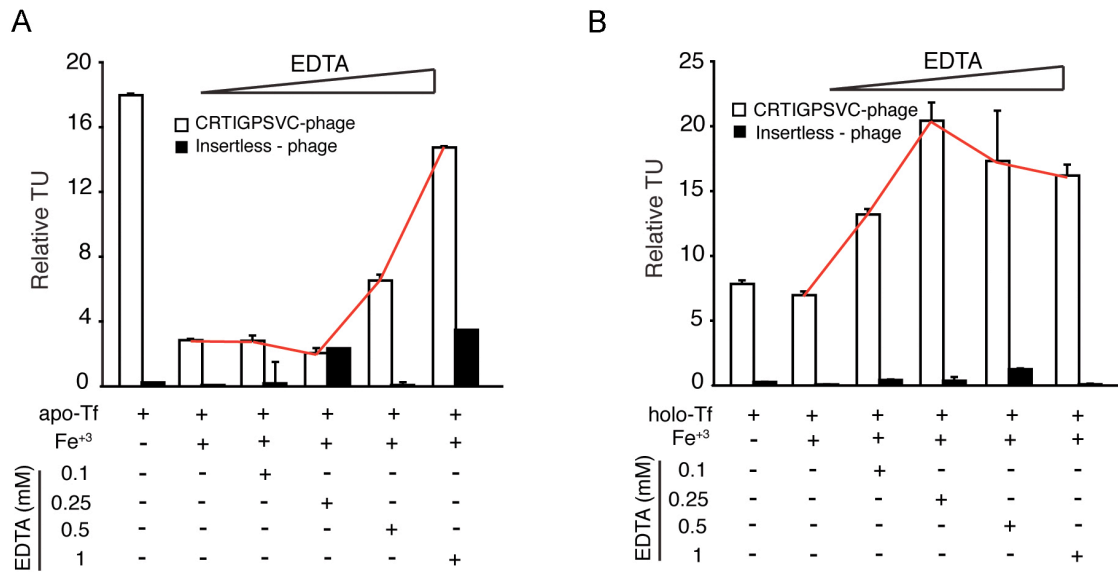


Figure 14. EDTA-mediated chelation abolishes phage binding to apo-transferrin. The effect of iron on the binding of phage to apo-transferrin was reversed by EDTA, but no effect was observed with holo-transferrin. In vitro binding assays were performed in 96-well plates coated with either apo-transferrin (A) or holo-transferrin (B), in the presence of iron and increasing amounts of EDTA.

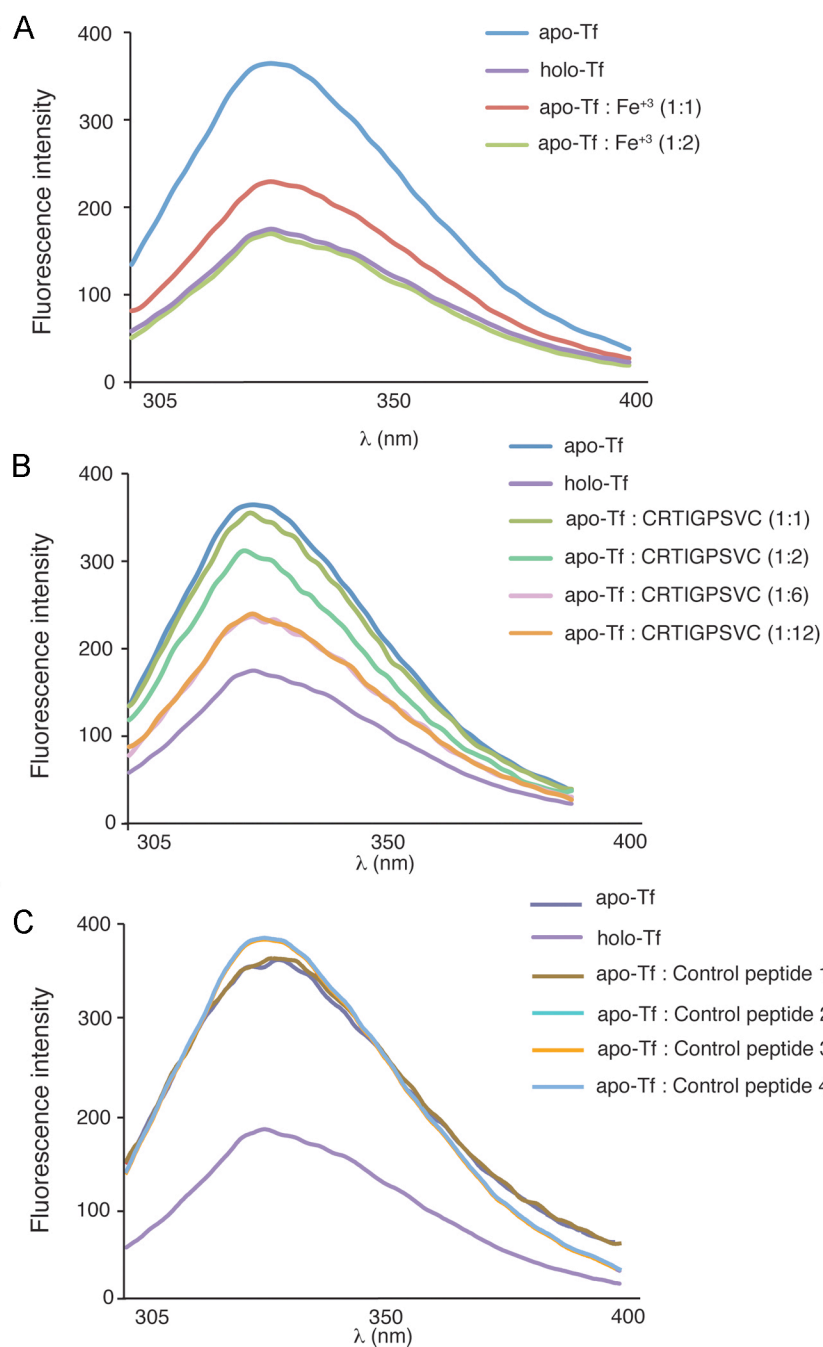


Figure 15. CRTIGSPVC peptide-induced conformational change assessed by steady-state fluorescence analysis. Steady-state emission spectra of apo-Tf in the presence of iron (A) or distinct concentrations of the CRTIGPSVC peptide (B). Four different peptide sequences (C) were used as control. Control peptide 1: CGLPYSSVC; Control peptide 2: CSGIGSGGC; Control peptide 3: CRFESSGGC; and Control peptide 4: CPQRGVTPC.

peptide (**Fig. 15B**); under these experimental conditions, the interaction reached saturation at 1:6 molar ratio (apo-Tf:CRTIGPSVC). Finally, a panel of unrelated control peptides served to demonstrate that the phenomenon is specific to the interaction between apo-Tf and CRTIGPSVC (**Fig. 15C**). Consistent experimental results were obtained with another optical method, circular dichroism (CD) analysis (**Fig. 16**). As expected, adding Fe^{+3} to apo-Tf generated a shift in the spectra reflecting the known iron-induced conformation change from apo-Tf to holo-Tf (**Fig. 16A**) (107-109). The CRTIGPSVC peptide also mediated conformation changes in apo-Tf (**Fig. 16B**), with no such changes detected with addition of unrelated control peptides (**Fig. 16C**). Together, these data (**Figs. 15 and 16**) strongly suggest that the CRTIGPSVC peptide mediates a protein conformational change in apo-Tf. One should note that, unlike iron, the peptide does not appear to mediate a full conformational change from apo-Tf to holo-Tf. Thus, further studies will be required to understand the precise nature of this peptide-protein interaction.

Chapter 3.3: CRTIGPSVC-phage targets Tf:TfR *in vivo*.

Because CRTIGPSVC-phage binds to apo-Tf *in vitro*, and the CRTIGPSVC peptide changes the conformation of apo-Tf in a concentration-dependent manner, we next asked whether the same mechanism would be implicated in the homing and transport of phage particles across the BBB *in vivo*. Moreover, as the over-expression of TfR has been suggested in primary brain tumors (46, 110), and as TfR has the highest gene expression ratio in glioblastoma compared to normal brain (9) (**Table 1**), we chose to study the targeting properties of CRTIGPSVC-phage in an orthotopic model of human-derived glioblastoma multiforme (46, 47, 86, 110).

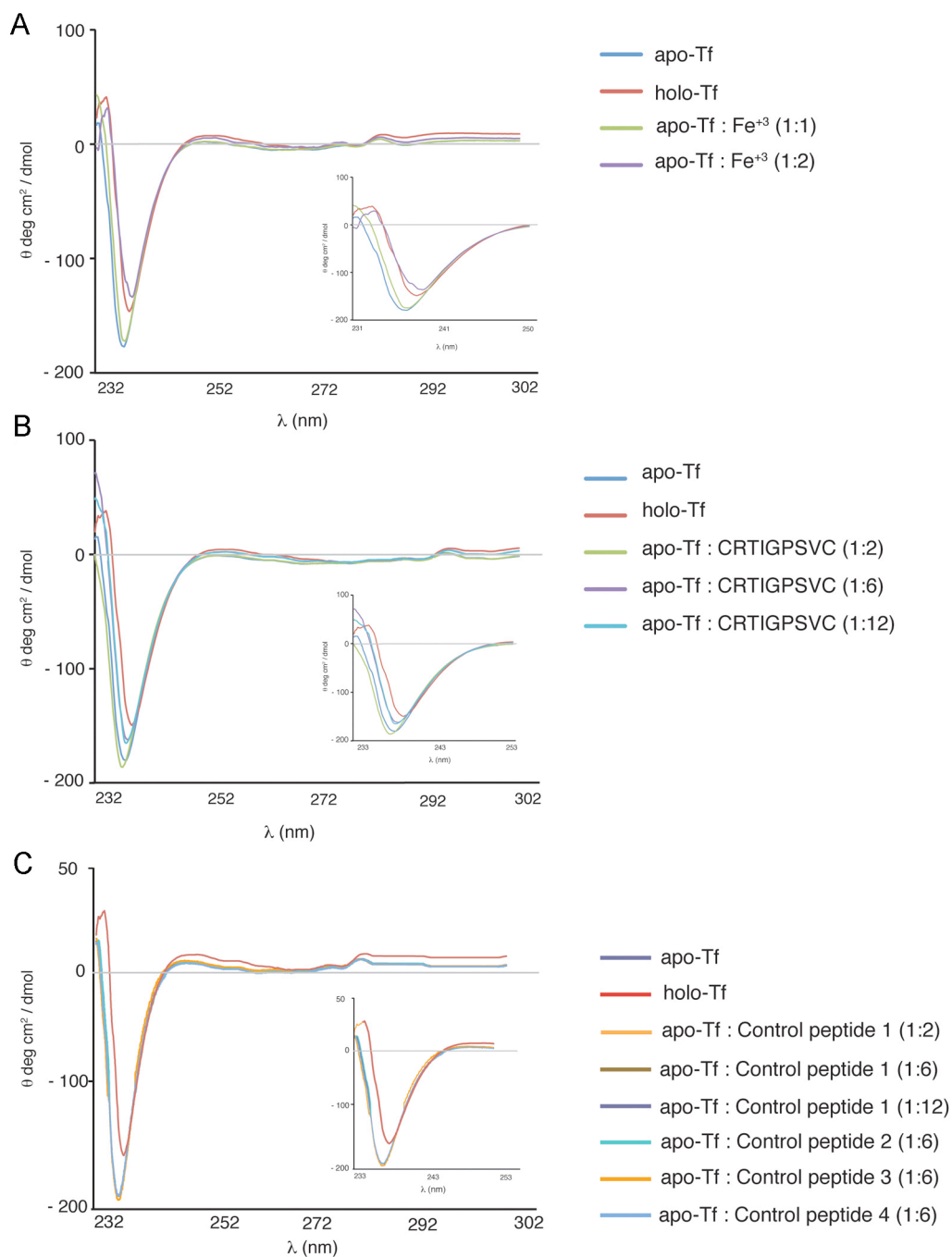


Figure 16. CRTIGSPVC peptide-induced conformational change assessed by circular dichroism analysis. Near UV-CD spectra of apo-transferrin in the presence of iron (A) or distinct concentrations of the CRTIGPSVC peptide (B). Four different peptide sequences (C) were used as controls. Control peptide 1: CGLPYSSVC; Control peptide 2: CSGIGSGGC; Control peptide 3: CRFESSGGC; and Control peptide 4: CPQRGVTPC. Insets show CD spectral region between 230 and 250 nm.

Table 1: Expression of RMTs in GBM compared to normal brain (NB)

Affymetrix ID	Gene Symbol	Gene Title	Ratio GBM/NB	P-value (t-test)
208691_at	TFRC	Transferrin receptor (p90, CD71)	2.1	3.83E-33
202068_s_at	LDLR	Low density lipoprotein receptor	1.6	1.02E-05
207332_s_at	TFRC	Transferrin receptor (p90, CD71)	1.4	1.91E-27
202067_s_at	LDLR	Low density lipoprotein receptor	1.1	0.033619
209894_at	LEPR	Leptin receptor	1.0	0.702604
217183_at	LDLR	Low density lipoprotein receptor	1.0	0.039231
217103_at	LDLR	Low density lipoprotein receptor	1.0	0.002134
217173_s_at	LDLR	Low density lipoprotein receptor	0.9	0.122683
217005_at	LDLR	Low density lipoprotein receptor	0.9	0.125734
207851_s_at	INSR	Insulin receptor	0.8	0.003325
207255_at	LEPR	Leptin receptor	0.8	0.046729
211354_s_at	LEPR	Leptin receptor	0.7	0.738849
211355_x_at	LEPR	Leptin receptor	0.7	0.075484
211356_x_at	LEPR	Leptin receptor	0.6	0.058692

Gene expression ratio of RMTs in GBM versus NB is shown from the highest (TFRC) to lowest (LEPR) level of relative gene expression.

First, to establish whether the U87-MG-derived xenograft would serve as a suitable model, we compared the expression of TfR in normal brains and in human glioma xenografts by fluorescence immunohistochemistry (**Fig. 17**). CD31 (PECAM-1) was used as a standard vascular marker (**Fig. 17A and D**). While the expression of TfR was moderate and restricted to blood vessels in the normal brain (**Figure 17A to C**), we observed robust expression of TfR in both tumor blood vessels (arrows) and tumor stroma (arrowheads) (**Figure 17D to F**). These data established that the human-derived malignant glioma xenografts were an appropriate experimental system for the study of Tf:TfR:peptide-mediated phage targeting and delivery *in vivo*. Next, the binding capacity and targeting properties of the CRTIGPSVC-phage were compared in normal tissue and tumor. Tumor-bearing animals were iv administered with phage, and tumor and contralateral brain hemisphere (normal tissue) were collected after 10 min, 30 min, and 1 h of systemic circulation (**Fig. 18**). We obtained coronal brain sections (each ~1 mm thick), isolated total DNA and amplified phage DNA for localization. We also obtained muscle, pancreas, liver, lung, spleen, and kidney as control organs (**Fig. 19**). Representative photomicrographs of hematoxylin and eosin (H&E)-stained brain slices illustrate brain structures present in coronal sections from which total DNA was recovered (**Fig. 18A**). Quantitative real-time PCR was then used to measure the levels of phage particles present in normal brain tissue compared to tumor samples and control organs. After 10 min of circulation, high levels of the CRTIGPSVC-phage were observed in each normal brain slice whereas control insertless phage was not detected. In contrast, comparable levels of both targeted and insertless phage were obtained in tumor (**Fig. 18B, boxed**). However, after 30 min, the same amount of targeted phage was detected in the tumor while the number of phage particles in normal

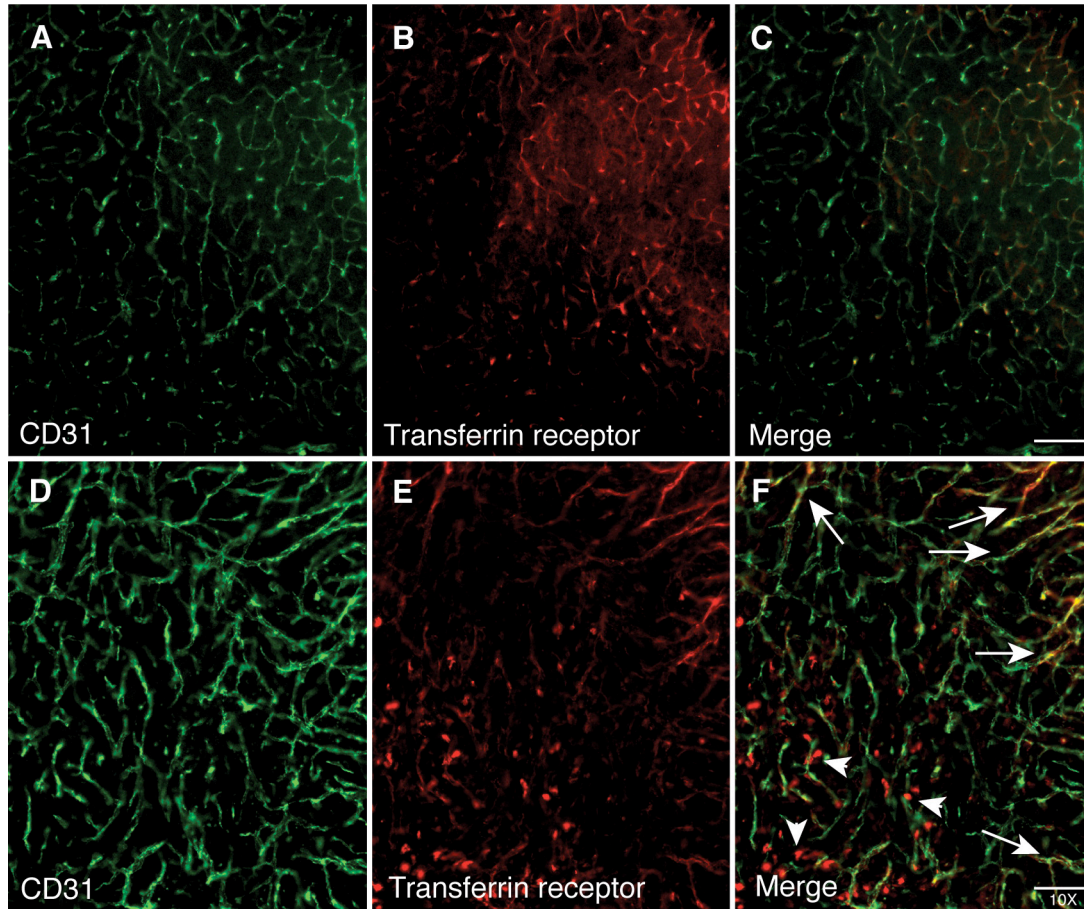


Figure 17. Expression of transferrin receptor in normal brain and human glioblastoma xenograft. (A to F) CD31 (green) and transferrin receptor (red) immunofluorescence demonstrate expression of TfR in both normal (A to C) and tumor tissues (D to F). (E) High levels of expression of TfR, in parallel with the increased capillary density are observed in brain tumor. (F) Merged image shows co-localization of TfR and CD31 in angiogenic blood vessels of human glioblastoma xenografts. Arrow: tumor blood vessels; arrowhead: tumor parenchymal cells.

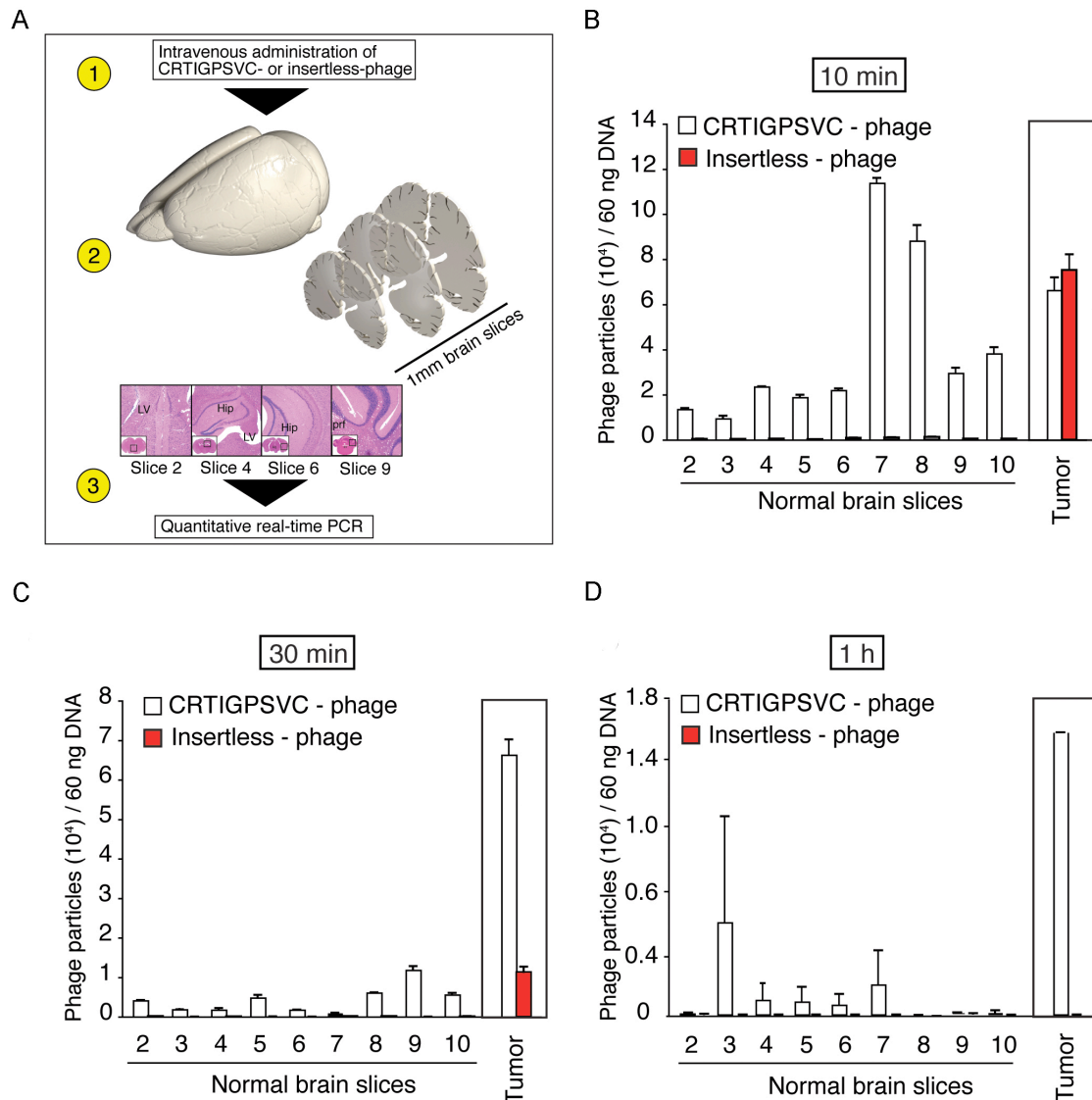


Figure 18. CRTIGPSVC-phage targets orthotopic brain tumors. (A) Schematic representation of brain slicing technique and quantitative real-time PCR used to demonstrate that CRTIGPSVC-phage crosses the BBB. Step 1: Phage was injected intravenously into tail veins of mice. Step 2: Brain and control organs were collected. Coronal brain slices 1 mm thick were obtained with the aid of a brain-slicer mold. H&E-stained sections illustrate prominent tissue components: the lateral ventricle (LV, slice 2), hippocampus (Hip, slices 4 and 6), and cerebellum (slice 9). Step 3: Total DNA of each brain slice was purified and used as template for phage DNA amplification and quantification by quantitative real-time PCR. (B to D) Quantification of phage homing to tumor and normal brain after 10 min (B), 30 min (C) and 1 h (D) of systemic circulation.

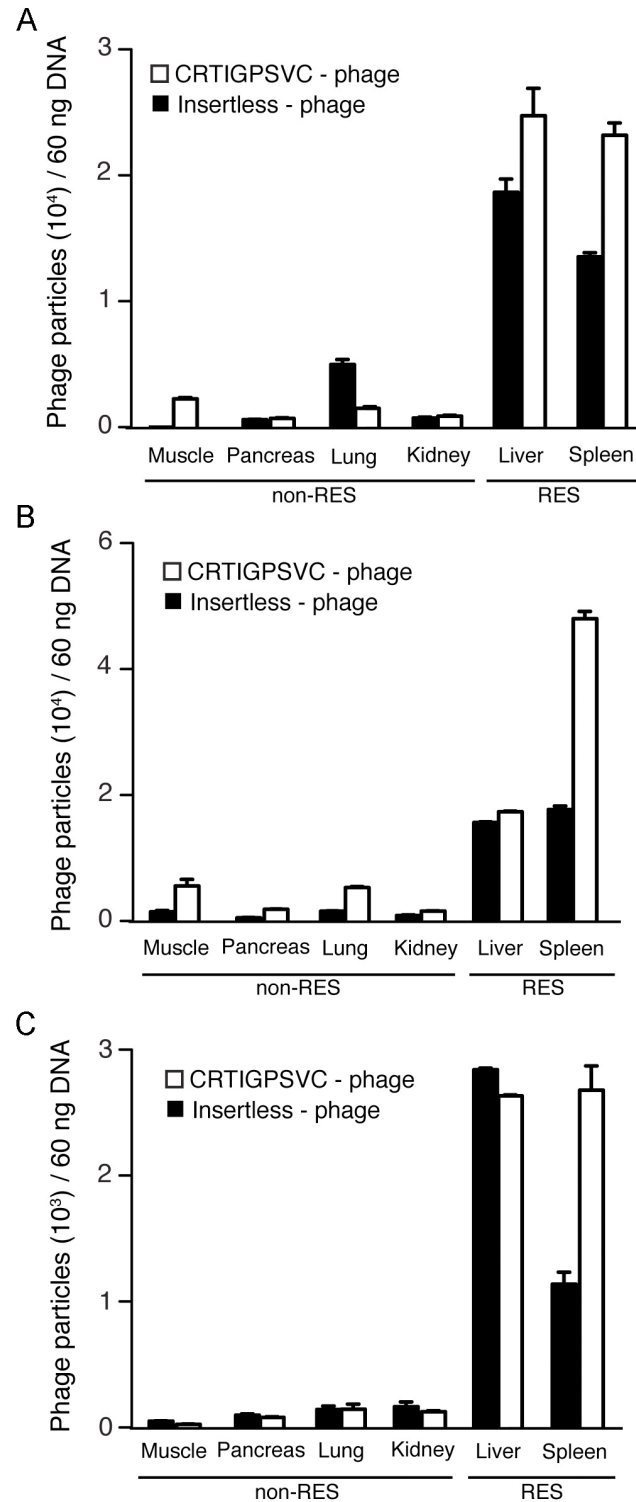


Figure 19. Homing of CRTIGPSVC-phage and insertless phage to non-CNS control organs. Mice were injected with 10^{10} TU of phage and organs were collected after 10 min (A), 30 min (B), and 24 h (C) of systemic circulation. RES, reticulo-endothelial system.

brain slices was markedly reduced. Notably, insertless phage was not observed in either tumor or normal brain (**Fig. 18C**). At 1 h post targeted phage administration, we detected $\sim 1.6 \times 10^4$ TU/60 ng DNA in the tumor (**Fig. 18D, boxed**), whereas normal brain tissue and insertless phage showed phage DNA only at background levels. In support of our original findings, pharmacokinetic studies of phage half-life in blood illustrated little difference between CRTIGPSVC-phage and insertless phage in animals bearing orthotopic brain tumors (**Fig. 20**). To confirm tumor targeting specificity, we assessed CRTIGPSVC-phage localization in mice bearing subcutaneous human xenografts after 10 and 30 min of systemic circulation, compared to control phage (**Fig. 21A**). Of note, the number of targeted phage particles recovered in subcutaneous tumors was ~ 10 -fold lower than that obtained in intracranial tumors given the same injection titer; this result suggests that potentially more than one targeting mechanism may be involved in the setting of a compromised BBB. Moreover, we observed phage accumulation in the spleen and liver of mice at all time points (**Fig. 19**), a result of the long-established pattern of non-specific particle clearance in the reticulo-endothelial system (66, 67, 111). Finally, similar to data obtained from the orthotopic model, pharmacokinetic studies showed no difference in the circulation half-lives of peptide-targeted phage versus control phage in mice bearing subcutaneous tumors (**Fig. 21B**). Clearly, a distinct phage distribution profile is obtained in brains with tumor, a result indicative that phage-targeting properties are largely dictated by receptor expression and accessibility to the circulating ligand peptide (112). Additional known factors such as increased vascular permeability leading to increased retention within tumors and increased activity of tumor endothelium contribute to the enhanced targeting by CRTIGPSVC-directed phage particles (112, 113). Future studies will be required to elucidate the relative

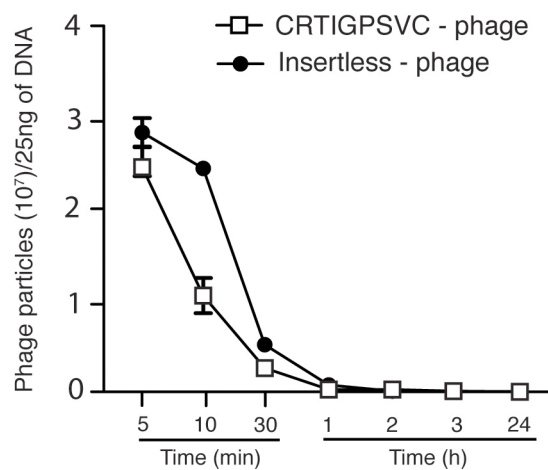


Figure 20. Pharmacokinetic study of blood half-life for CRTIGPSVC and insertless phage in tumor bearing mice. CRTIGPSVC-phage and insertless phage were administered into mice bearing intracranial tumors and the half-life in blood was established. Data depict similar clearance irrespective of the presence of an insert peptide.

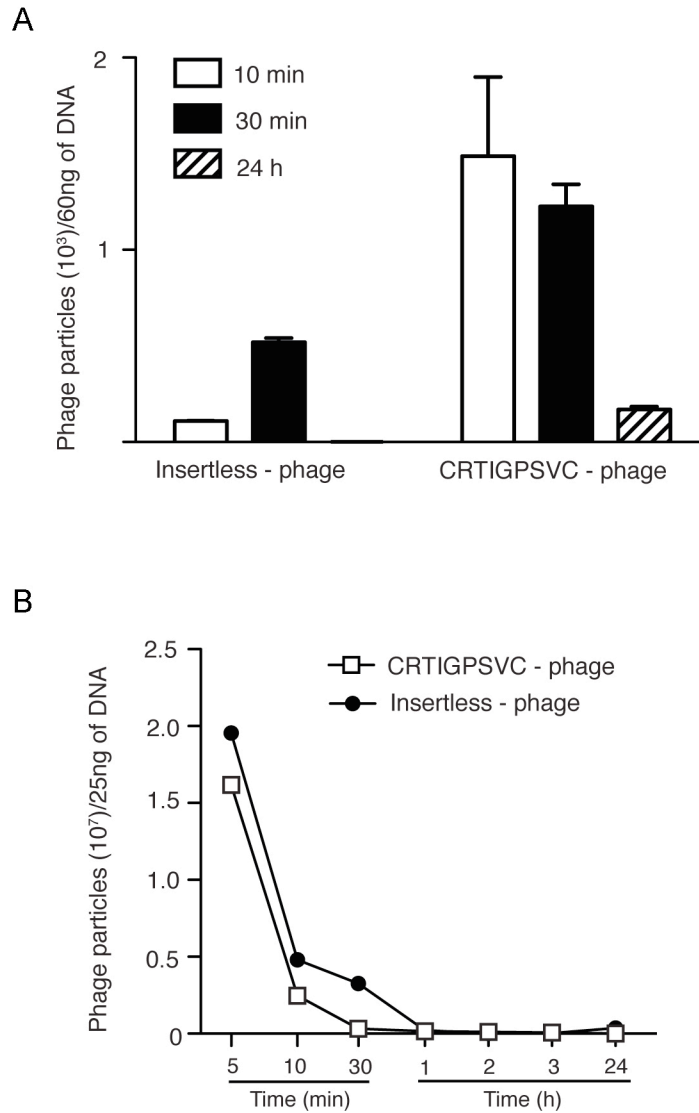


Figure 21. CRTIGPSVC-phage targets subcutaneous brain tumor xenografts. (A) Tumor bearing mice were administered with targeted CRTIGPSVC-phage or insertless phage. Control organs and tumors were collected after 10 min, 30 min, and 24 h of systemic circulation. (B) Pharmacokinetic study of the half-life of CRTIGPSVC- or insertless phage in blood.

contribution of each individual non-mutually exclusive mechanism(s) in the peptide-mediated brain tumor selectivity.

To evaluate CRTIGPSVC-phage localization, we next used immunohistochemistry to detect phage within tumors. Immunohistochemistry revealed specific, punctate staining of phage within the tumor vasculature (**Fig. 22A**). Strong immunostaining of phage particles was also detected in the tumor parenchyma, data demonstrating passage of CRTIGPSVC-phage from glioma-associated blood vessels to tumor cells (**Fig. 22B to E, arrowheads**). We observed no phage staining in tumors from animals injected with insertless phage (**Fig. 22F**) as well as little phage detected in unrelated regions of the brain, such as cerebral cortex (**Fig. 22G**) and caudate/putamen (**Fig. 22H**). Next, given the vascular localization of CRTIGPSVC-phage, we used fluorescence immunohistochemistry in thick (60-80 μ m) frozen tissue sections to visualize the distribution of phage within the CD31 positive vasculature in three-dimensions (**Fig. 23**). CRTIGPSVC-phage was widely and homogenously distributed within the tumor vasculature but not the blood vessels of normal tissue at 30 min (**Fig. 23A to C**). At the same timepoint, no signal was exhibited by insertless phage within either the tumor or normal brain tissue (**Fig. 23D to F**).

By confocal microscopy, we confirmed the CRTIGPSVC-phage targets and co-localizes with cells expressing the transferrin receptor. Thick sections of frozen brain from tumor-bearing animals systemically receiving CRTIGPSVC-phage iv were analyzed for the presence of CD31 (**Fig. 24A**), TfR (**Fig. 24B**), and phage (**Fig. 24C**); TfR and phage immunoreactive particles were found to coincide with blood vessels (**Fig. 24D**). Moreover, CRTIGPSVC-phage and TfR colocalized with tumor parenchymal cells (**Figure 24E**,

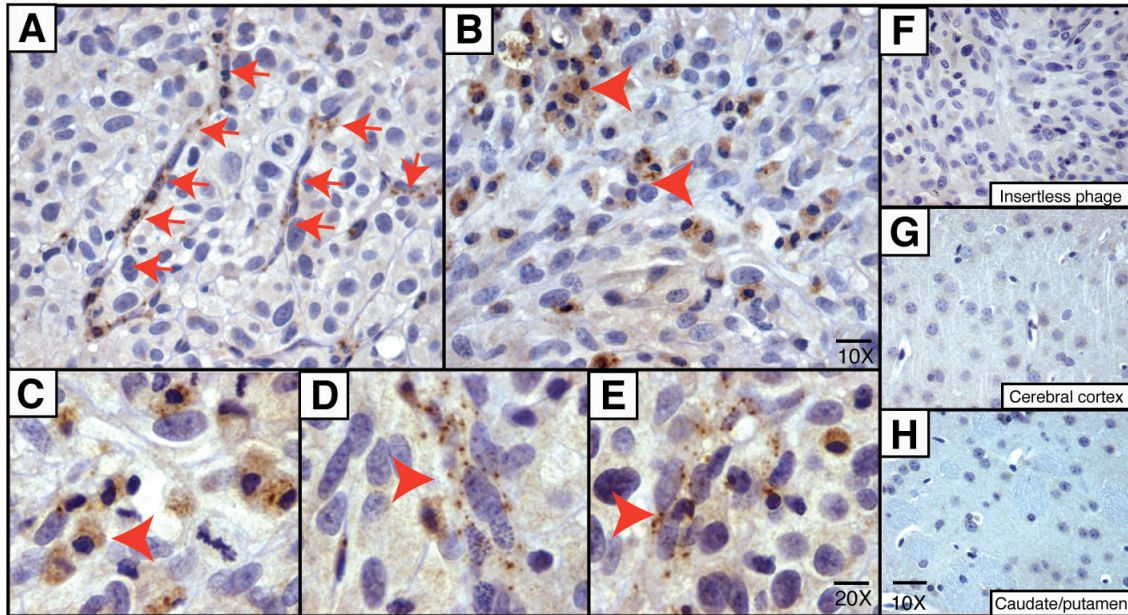


Figure 22. CRTIGPSVC-phage targets human glioblastoma in vivo.

Immunohistochemistry of CRTIGPSVC-phage after systemic circulation into human-derived glioblastoma xenograft-bearing mice. Staining of phage was observed in tumor blood vessels (A; arrows) and glioma cells (B to E; arrowheads). (F) Insertless phage was used as a negative control. Other areas of the brain such as (G) cerebral cortex and (H) caudate/putamen showed only background staining.

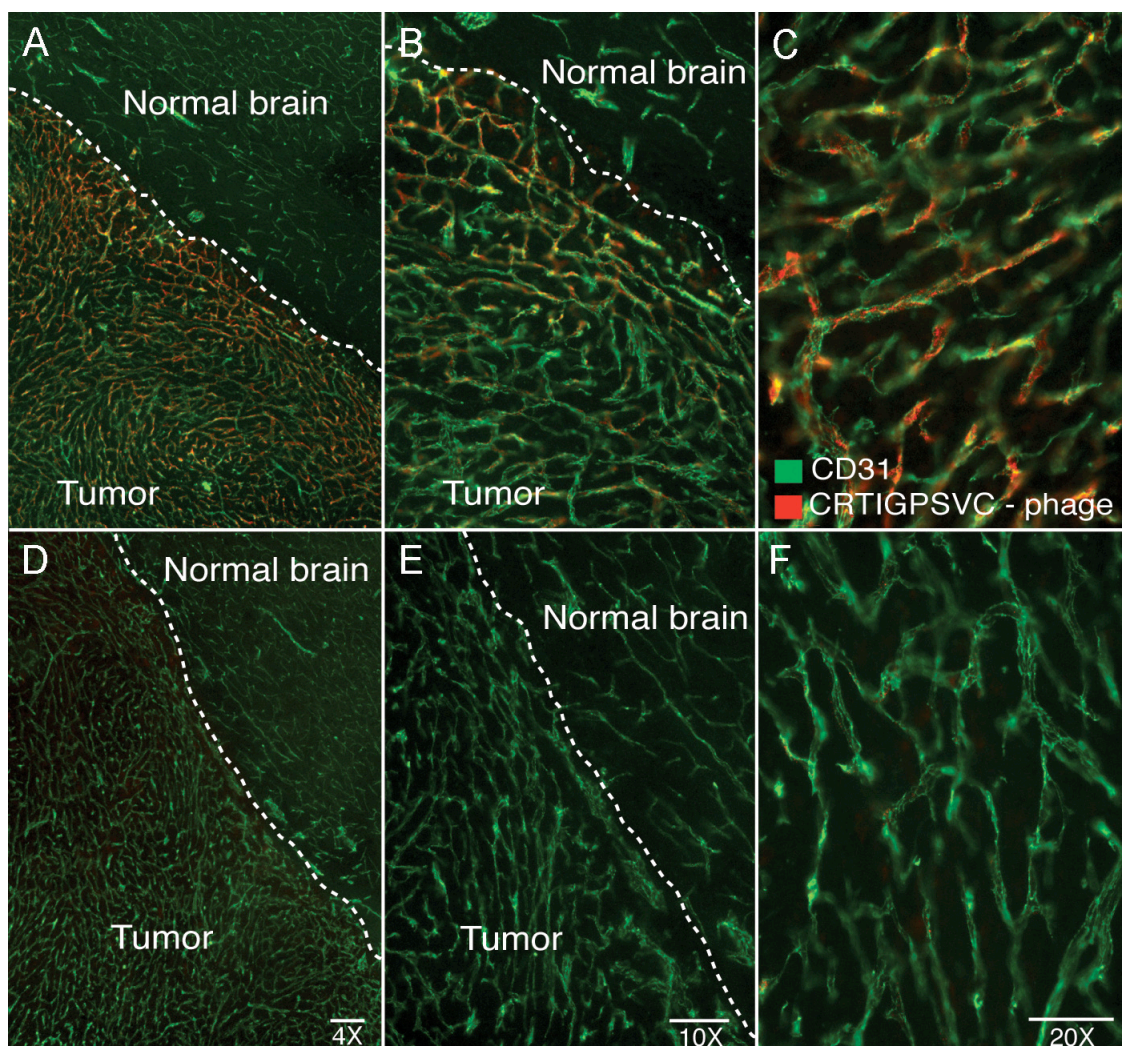


Figure 23. CRTIGPSVC-phage localizes to tumor blood vessels.

Immunofluorescence of phage (red) and CD31 (green) revealed accumulation of CRTIGSPVC-phage particles in tumor blood vessels but not in normal tissue (A to C). Insertless phage, used as a negative control, revealed little or no staining (D to F).

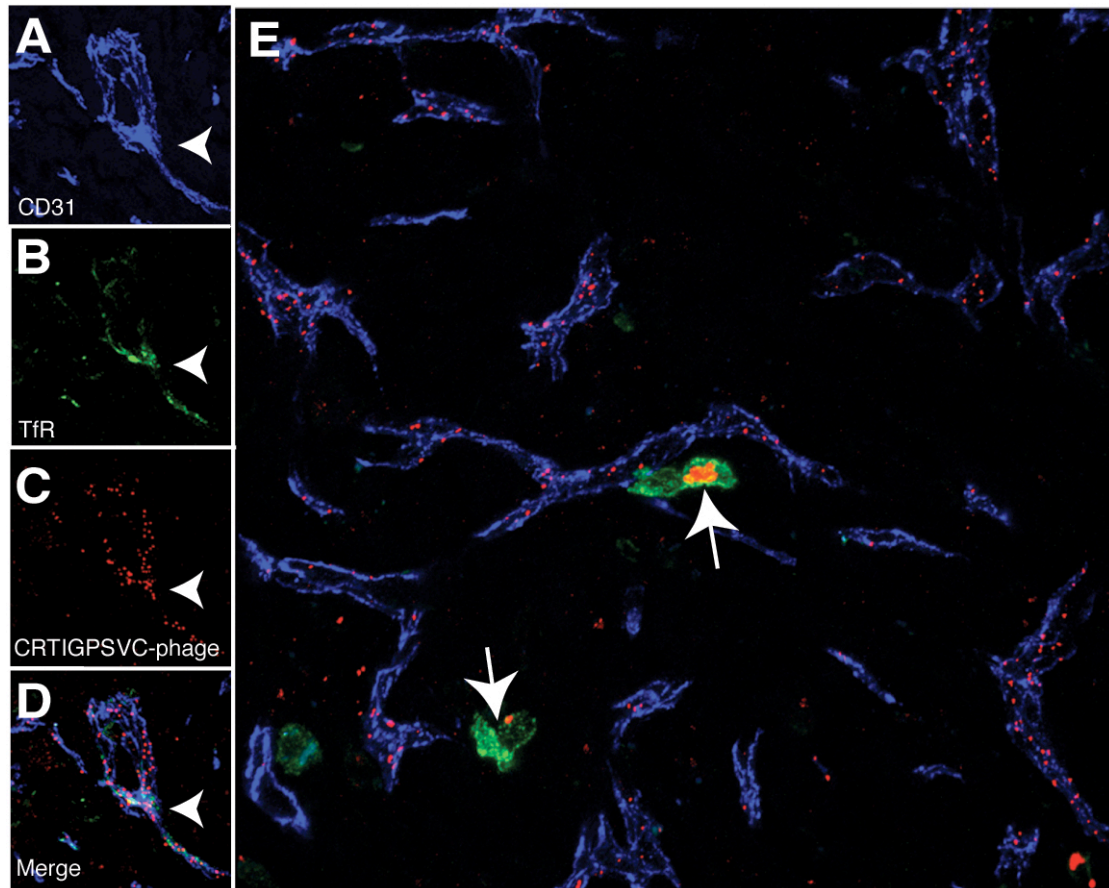


Figure 24. CRTIGSPVC-phage co-localizes with transferrin receptor in tumors. Confocal fluorescence microscopy showed co-localization of (A) CD31, (B) transferrin receptor, and (C) phage in blood vessels. (D) Merge of images (A to C). Arrowheads point to protein co-localization. (E) Phage particles co-localized to transferrin receptor-expressing cells in the tumor parenchyma (arrows).

arrows), consistent with the interpretation that the mechanism by which CRTIGPSVC-phage binds and translocates into the tumor vasculature is mediated by the Tf:TfR protein complex.

Chapter 3.4: Targeted transgene delivery and molecular imaging of brain tumors.

We showed that CRTIGPSVC-phage preferentially targets TfR-expressing cells and demonstrated that transport of phage into normal brain and brain tumor vasculature is likely mediated by the Tf:TfR molecular complex. Next, to begin to examine the translational potential of this discovery, we generated a CRTIGPSVC-displaying AAVP vector to merge gene delivery and molecular imaging in an orthotopic preclinical model of human glioma (77-79, 82, 114). A CRTIGPSVC-AAVP construct carrying the *Herpes simplex virus thymidine kinase* gene (*HSVtk*) was engineered; the *HSVtk* transgene can serve as both a suicide gene strategy when combined with drugs such as ganciclovir (GCV) or as a reporter for molecular-genetic imaging of tracers such as [¹⁸F]-FEAU (77, 79, 80). We delivered CRTIGPSVC-AAVP-*HSVtk* or control insertless-AAVP-*HSVtk* to cohorts of brain tumor-bearing mice (n=10/group). Animals treated with vehicle were also used as controls (n=10). Both CRTIGPSVC-AAVP and insertless-AAVP groups were treated with GCV for 5 days (80 mg/kg/day, ip) and response to treatment was assessed by measurement of tumor areas (**Fig. 25**) and by histopathological examination (**Fig. 26**). After GCV-based therapy, the size of tumors in mice that received CRTIGPSVC-AAVP-*HSVtk* was significantly smaller (Student's *t* test, *p*<0.001) than that in mice receiving insertless-AAVP-*HSVtk* or vehicle alone (**Fig. 25**). Immunohistochemical studies for CD31 expression demonstrated that systemic administration of CRTIGPSVC-AAVP-*HSVtk* followed by GCV therapy caused

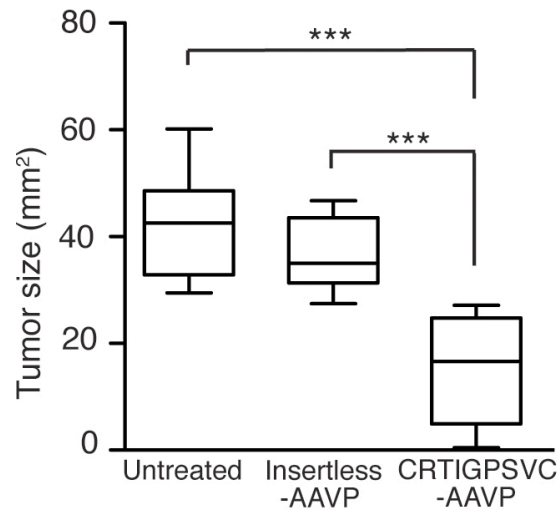


Figure 25. Targeted therapy of an orthotopic model of human-derived glioblastoma xenograft. Tumor growth suppression by CRTIGPSVC-AAVP-*HSVtk* transduction plus treatment with ganciclovir (GCV). Cohorts of immunodeficient nude mice (n=10) with established intracranial tumors derived from U87-MG cells received a single systemic administration of targeted CRTIGPSVC-AAVP-*HSVtk* (5×10^{10} TU) or control insertless-AAVP-*HSVtk*. Mice received GCV from 7 d post systemic iv AAVP administration until the end of the experiment (daily GCV dose ip for 5 d). Untreated group received vehicle alone. Shown are the means of tumor area \pm standard deviations (SD) and a statistically significant reduction in tumor volume was observed with CRTIGPSVC-AAVP therapy (***Student's *t* test, $p < 0.001$).

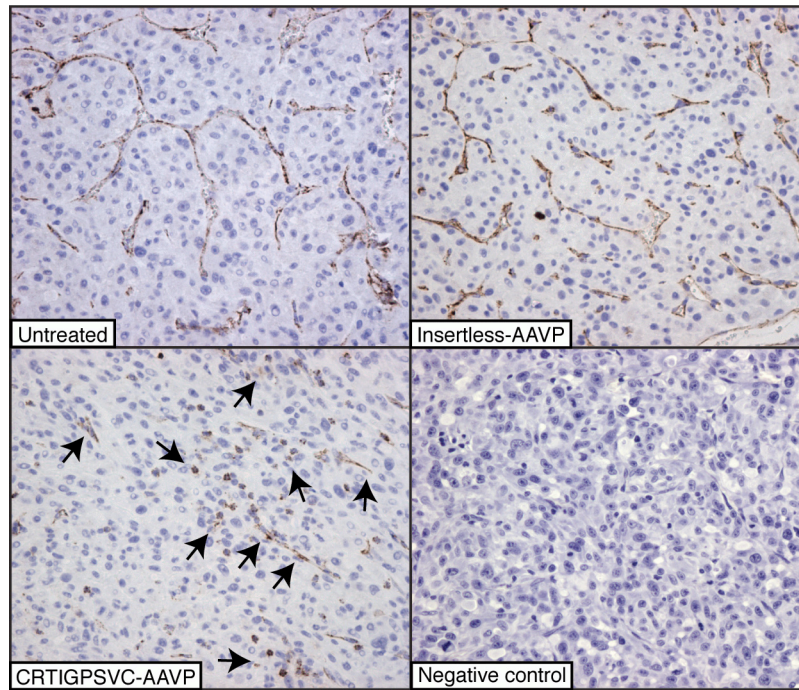


Figure 26. Histopathologic analysis of brain tumors following targeted therapy. CD31 staining was performed on paraffin embedded brain tumor tissue sections of animals treated with CRTIGPSVC-AAVP or control insertless-AAVP. Untreated animals received only vehicle. Arrows point to disrupted blood vessels. Negative control: tumor tissue stained with IgG control isotype.

targeted destruction of capillary-like blood vessels, in line with immunohistochemical data obtained in our experimental model of glioblastoma multiforme (**Fig. 26**). This effect was not observed in animals treated with insertless-AAVP or vehicle. Next, we tested the efficacy of clinically applicable molecular-genetic PET imaging with [^{18}F]-FEAU combined with CT scan imaging for noninvasive monitoring of the cellular dynamics and heterogeneity of *HSVtk* reporter gene expression in living orthotopic glioma-bearing mice (**Fig. 27**). PET imaging with [^{18}F]-FEAU was performed 7 d and 10 d after vector administration to assess the localization and magnitude of *HSVtk* expression. No specific transgene expression was detected 7 d after AAVP administration iv (data not shown). In contrast, we observed significant (Student's *t* test, $p < 0.05$) levels of *HSVtk* expressed as relative tumor/muscle injected dose/gram (ID/g) after 10 d in the tumors of animals administered with CRTIGPSVC-AAVP-*HSVtk* compared to the control group (**Fig. 27A**). Combined micro-PET/CT images in axial, coronal, and sagittal planes in tumor-bearing mice revealed heterogeneous targeting of intracranial human glioblastoma xenografts with little or no signal in the normal brain tissue (**Fig. 27B**), whereas control insertless-AAVP yielded negative results in both normal brain and tumor (**Fig. 27C**); these data were consistent with our immunohistochemical stainings following phage administration. Finally, terminal deoxynucleotidyl-transferase-mediated dUTP-biotin nick end labeling (TUNEL) staining clearly confirmed a heterogeneous distribution of apoptotic endothelial and glioma cells within the tumor but little to no apoptosis observed in tumors from mice that received either insertless-AAVP-*HSVtk* or vehicle alone (**Fig. 28A to D**). Together, these results demonstrate that the level of *HSVtk* transgene expression in human glioblastoma xenografts is sufficient for effective GCV activation.

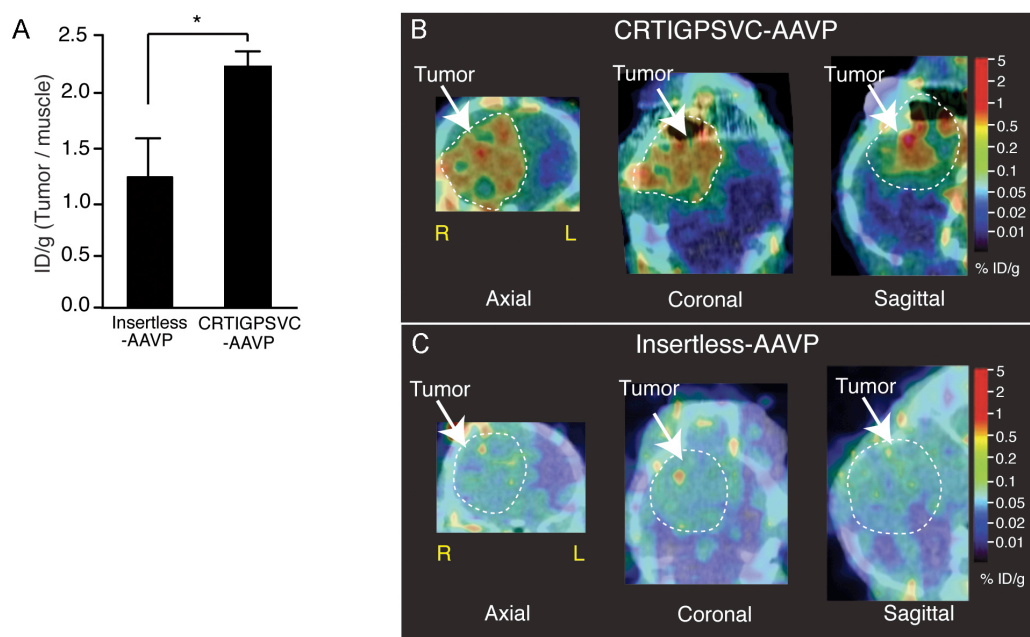


Figure 27. Targeted molecular-genetic imaging of intracranial brain tumors. (A) Temporal dynamics of HSVtk gene expression as assessed by micro-PET imaging with [^{18}F]-FEAU. Significant HSVtk expression (*Student's t test, $p < 0.05$) 10 d after systemic administration was observed with CRTIGPSVC-AAVP compared to control insertless-AAVP. (B and C) Combined PET/CT images of brain tumor-bearing animals systemically administered with targeted CRTIGPSVC AAVP-*HSVtk* (B) or control insertless AAVP-*HSVtk* (C). Axial, coronal, sagittal planes are shown. [^{18}F]-FEAU uptake was observed only in animals receiving CRTIGPSVC-AAVP. Arrows point to the tumor area. R, right; L, left.

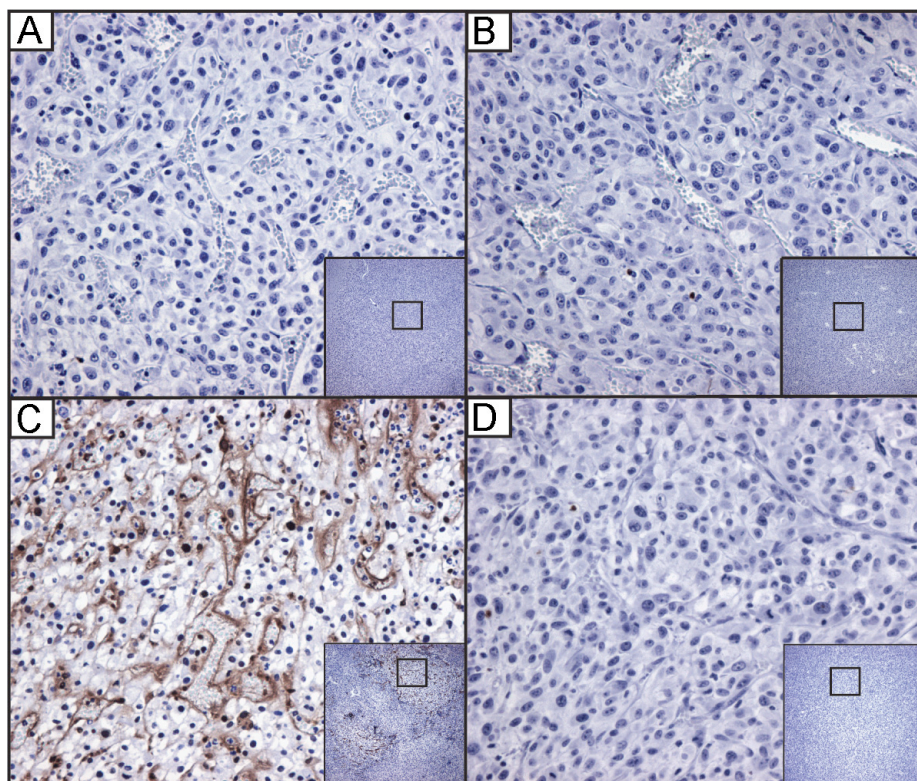


Figure 28. Tumor apoptosis by CRTIGPSVC-AAVP therapy. Detection of apoptotic cells by TUNEL was performed on tumor tissue sections of animals treated with control insertless-AAVP (B) or with CRTIGPSVC-AAVP (C). (A) Untreated animals received only vehicle. (D) Non-immune IgG control. Low magnification insets of serial tumor sections demonstrate the area containing the high-magnification views.

In order to assess the feasibility of this strategy for clinical applications, we used high-throughput glioma TMA samples to analyze the expression of TfR in a large (n=165) and comprehensive panel of primary human gliomas with well-annotated clinical and pathological features from the UTMDACC brain tumor bank (**Fig. 29A**). We first noted that small blood vessels were positive for TfR in the normal brain, a result consistent with the targeting properties of the CRTIGPSVC-phage observed in normal mouse brain (**Fig. 29B, arrows**). In GBM, the most common and aggressive primary brain tumor in humans, strong (3+) and moderate (2+) TfR staining was observed in tumor cells in 49 out of 56 (85%) analyzed samples (**Fig. 30**) (8, 115). Similarly, we observed strong (3+) and moderate (2+) in 4 out of 8 cases of gliosarcomas (GS; n=8; **Fig. 31A**) and 9 out of 26 cases of anaplastic astrocytomas (AA; n=26; **Fig. 31B**). In contrast, tumor cells were negative within the limits of our immunohistochemical procedures in low-grade oligodendrogliomas (O; n=28) (**Fig. 31C**), anaplastic mixed oligoastrocytomas (AMOA; n=11; not shown), mixed oligoastrocytomas (MOA; n=10; not shown), and anaplastic oligodendrogliomas (AO; n=22; not shown) samples. This patient-derived data set confirms that TfR is a suitable candidate target in GBM for translation into clinical applications and suggests potential expansion into other primary brain tumors.

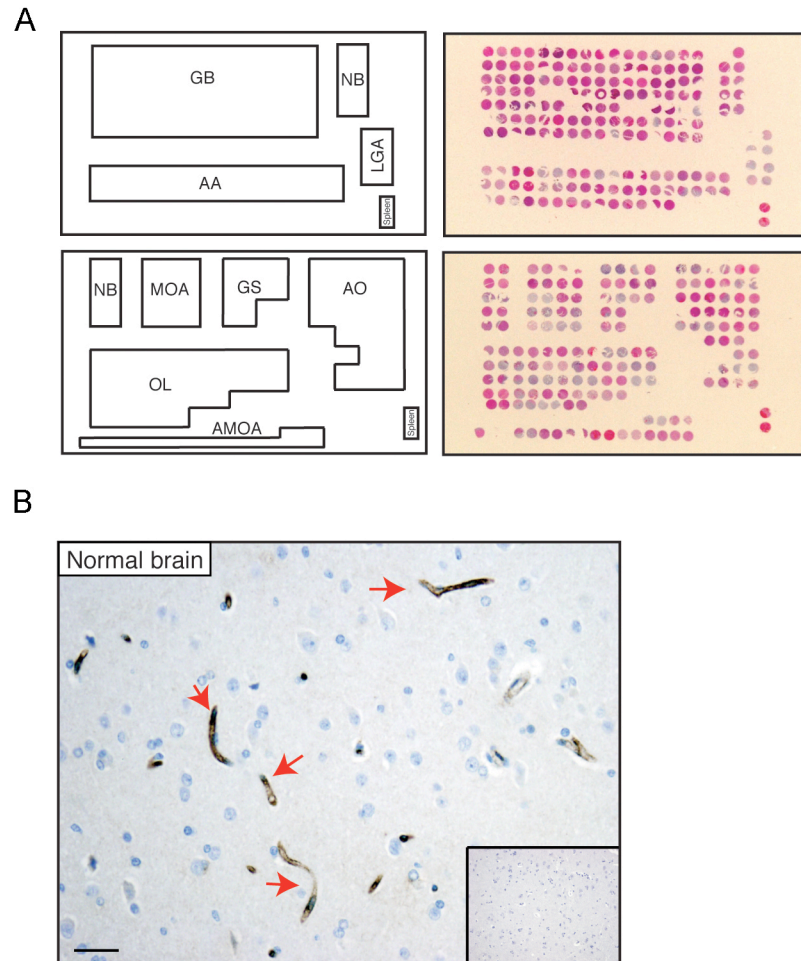


Figure 29. Transferrin receptor expression in comprehensive human glioma tissue microarrays. (A) Glioma tissue microarray maps and H&E-stained tissue sections. Abbreviations: AA, anaplastic astrocytoma; AO, anaplastic oligodendroglioma; AMOA, anaplastic mixed oligoastrocytoma; GM, glioblastoma multiforme; GS, gliosarcoma; LGA, low-grade diffuse astrocytoma; MOA, mixed oligoastrocytoma; NB, normal brain; O, oligodendroglioma. (B) Inset represents negative control.

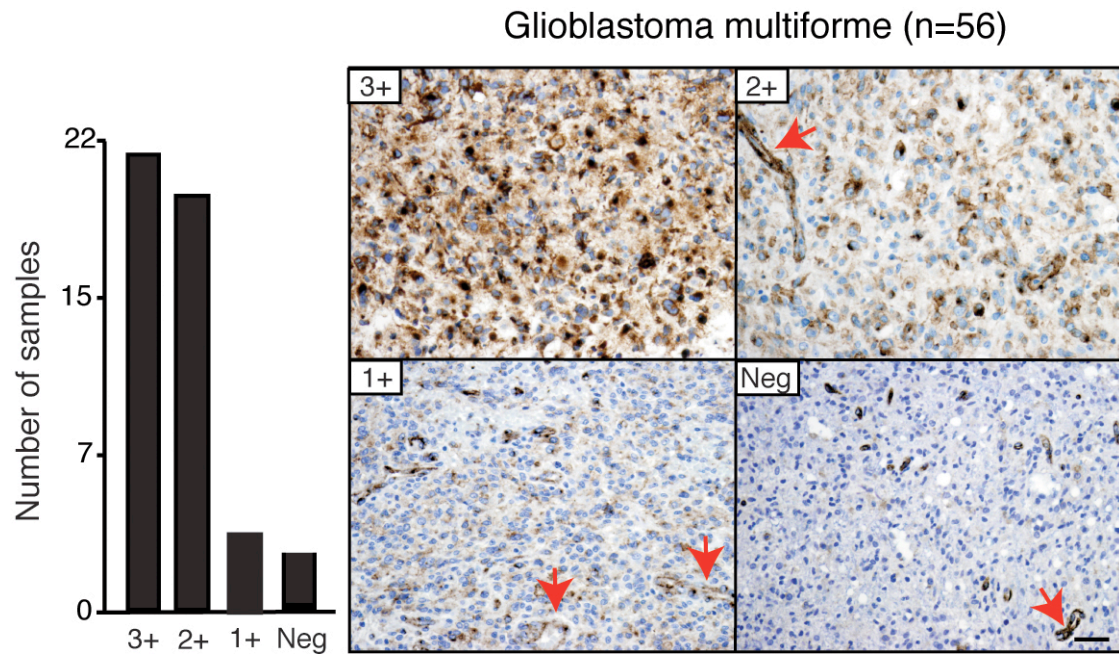


Figure 30. Transferrin receptor is highly expressed in glioblastoma. Tissue samples from 56 different patients were immunohistochemically stained for transferrin receptor and scored by a pathologist. Intense tumor cell (3+ or 2+) and vascular staining was noted in 49 of 56 samples. Pathology score for tumor cells: 3+: strong; 2+: moderate; 1+: weak. Arrows point to blood vessels.

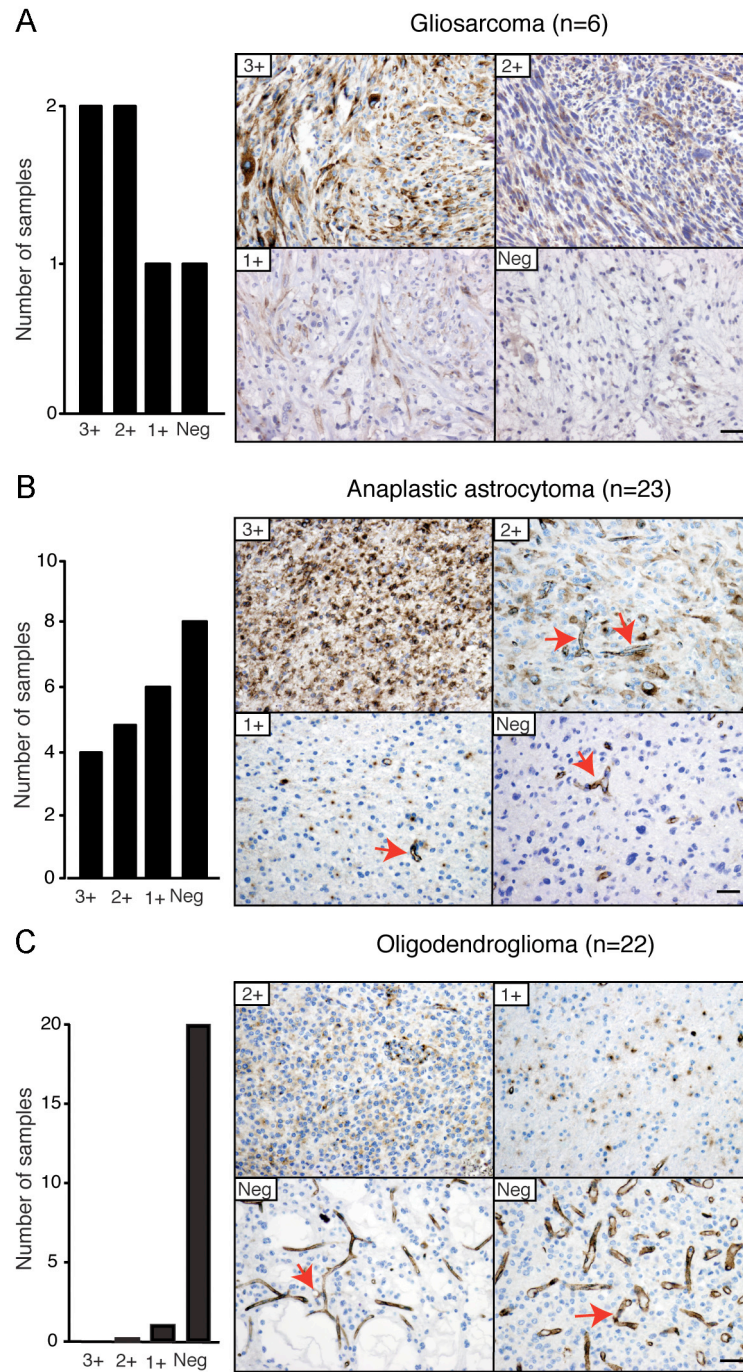


Figure 31. Transferrin receptor is expressed in primary human CNS tumors. Transferrin receptor is highly expressed in gliosarcomas (A) and anaplastic astrocytomas (B), but tumor cell reactivity was low in oligodendrogliomas (C). Arrows point to blood vessels.

CHAPTER 4: DISCUSSION

In summary, we show that a combinatorial phage display screening *in vivo* identified peptide ligands that localize to the brain following systemic administration. One of the identified peptides, CRTIGPSVC, demonstrated robust and specific brain targeting in a molecular complex involving transferrin and transferrin receptor. The peptide induced a partial conformational change in Tf, suggesting a similar but non-canonical iron-like interaction and a potential targeting mechanism. In a model of human glioma, a combination of TfR overexpression plus extended vascular permeability and ligand retention resulted in effective tumor targeting. Further, analysis of patient-derived human primary brain tumor specimens supports the concept that the CRTIGPSVC peptide and the TfR system may serve as a translational approach for the detection and treatment of GBM and other gliomas.

In vivo phage display screenings have successfully identified a number of vascular targeting ligands specifically localizing to both normal organs and tissue from angiogenesis related diseases (112, 116). The data support the physiological differences observed in capillary beds of various organs, in particular the endothelium of the brain, and predict that site-specific delivery exploiting molecular differences remains plausible. One of the unique advantages of *in vivo* screenings lies in peptide selection under native conditions. This functional screen identifies ligand-receptor interactions that are inherently accessible from the systemic circulation and allow for multi-protein complex formations that may be overlooked in isolated-protein or cell-based approaches. Thus, one might speculate that, given the identified interaction between the CRTIGPSVC peptide and Tf with TfR, this unique interacting complex would not have been isolated in another experimental setting. Moreover, to our knowledge, the induction of a conformational change in Tf similar to that of iron is unique to CRTIGPSVC and may not

have been functionally isolated *in vitro*. Together, these data exemplify the biological relevance of *in vivo* screening assays and support the utility of *in vivo* phage display for vascular targeting approaches.

Narrow therapeutic indices often limit the use and effectiveness of available treatments. The concept of targeted therapies suggests that traditionally cytotoxic agents could be specifically directed to diseased sites, allowing for increased local concentrations and limited systemic toxicity. One of the most well-studied and intensely developed systems has centered on the Tf:TfR interaction, particularly as a cancer therapy strategy, due to high TfR expression on actively dividing cells, efficient receptor internalization, and cell surface receptor localization (44, 45). Investigators have employed a number of strategies to exploit this system for delivery, including use of monoclonal antibodies against TfR, Tf fusion products, and Tf-directed viral and manufactured complexes, among others. The novelty of the work presented here lies in the use of a short peptide to mediate selective delivery rather than larger and bulkier antibodies, antibody fragments or Tf protein per se. Further study of the binding affinity, avidity, and pharmacokinetics of CRTIGPSVC compared to current Tf-related agents will ultimately determine whether this peptide-mediated approach will yield clear and consistent results in patients.

The precise structural details of iron binding to apo-Tf and the resultant conformational change induced by the binding event has been well studied. X-ray crystallography coupled with site-directed mutagenesis demonstrated that eight tryptophan (Trp) residues are intimately involved in iron binding to apo-Tf (43). Of note, a differential number of Trp residues are involved in binding to each lobe of apo-Tf, supporting the distinct association and dissociation profiles of iron with Tf. Three Trp residues (Trp8,

Trp128 and Trp264) form a coordination complex within the N-lobe with iron whereas five Trp residues (Trp344, Trp358, Trp441, Trp460 and Trp550) coordinate iron binding in the C-lobe. Given the intrinsic fluorescence characteristic of Trp, it was previously reported that assessment of changes in Trp fluorescence could be used to monitor iron-induced conformational changes in Tf (107-109). We were able to use steady state fluorescence (SSF) and circular dichroism (CD) analysis to demonstrate CRTIGPSVC-induced conformational changes in Tf, akin to iron (**Figs. 15 and 16**). However, as apo-Tf binds two iron (Fe^{3+}) ions, SSF and CD were unable to readily distinguish peptide-binding characteristics to each lobe of Tf. Similar studies could be performed with “locked” monoferric Tf molecules, such as use of a Tf with a point mutation of Arg 623 to alanine (TfR623A) to mimic the conformational change of iron binding to the C-lobe or a similar mutant mimicking an iron-bound N-lobe (TfK206E). Such mutants in previous studies determined that the N-lobe is sensitive to C-lobe conformation and relatively insensitive to TfR or pH, whereas the C-lobe is most sensitive to the presence of TfR and changes in pH (117). Thus, further analysis to elucidate the exact interacting lobe and binding residues will enhance understanding of the targeting dynamics of CRTIGPSVC and lead to future peptidomimetics with optimal binding characteristics.

The CRTIGPSVC-phage significantly accumulated in the brain as early as 10 minutes after systemic administration compared to the insertless control. Microvessel depletion analysis suggested that while the amount of phage retained within the vasculature for CRTIGPSVC-phage and the insertless control was similar at 10 minutes, CRTIGPSVC-mediated crossing of the normal BBB contributed to the total binding profile observed (**Fig. 9**). At 30 minutes, the data suggest that non-specific interactions with the brain endothelium are relatively cleared and

CRTIGPSVC-phage mediates specific binding to the cerebral blood vessels and crossing into the brain parenchyma. Thus, this time-dependent clearance and retention act in a coordinated fashion to mediate specific targeting by the normal brain. We have not yet systematically evaluated whether there is significant passage of AAVP or phage vectors from normal brain endothelial cells to parenchymal cells in the first min after administration. Further study of the temporal dynamics of CRTIGPSVC-phage-mediated crossing of the BBB, and thereby TfR cell surface internalization and recycling, will be critical in future development of this ligand-directed delivery system.

We observed an enhanced delivery efficiency of CRTIGPSVC-phage to human-derived intracranial brain tumors. The robust targeting was supported by enhanced TfR expression within the tumor, a function of both increased endothelial cell expression and microvessel density within the tumor. However, given the dynamics of CRTIGPSVC-mediated targeting, it remains likely that other parameters may ultimately influence tumor targeting, including circulation time, endothelial permeability, hydrostatic pressure, and receptor turnover rate. It also stands to reason that these factors may contribute to differences in the delivery of CRTIGPSVC-AAVP to normal mouse brain versus the grafted human brain tumors, where receptor accessibility and distribution within the tumor vasculature are likely crucial elements directing specific targeting. Of note, our studies utilized a single animal model of human glioblastoma, patient-derived U87-MG glioblastoma cells. While the model recapitulates important characteristics of human disease, it does not infiltrate surrounding brain tissue, a key feature of human GBM. It will be important to validate and extend pre-clinical study of CRTIGPSVC-mediated tumor targeting to additional models of intracranial brain tumors,

xenografts or transgenic models, to gain confidence for future success in translational applications.

Gene-directed enzyme prodrug therapy approaches, including suicide-gene therapy with *HSVtk*, afford the unique ability to non-invasively monitor delivery and transduction efficiencies, gene expression profiles over time, and efficacy of therapies with a single agent. Two critical aspects to be addressed for successful application of this methodology are use of well-characterized ligand-receptor pairs to drive specific localization and use of a gene delivery system enabling robust transgene expression. AAVP integrates such specific targeting ligands with a mammalian gene delivery system that is potentially highly adaptable to any ligand-receptor system through manipulation of the pIII targeting sequence. We demonstrated CRTIGPSVC-targeted AAVP carrying *HSVtk* allowed for tumor visualization by PET/CT with the radiolabeled nucleoside [^{18}F]-FEAU and therapy with GCV. A single administration of CRTIGPSVC-AAVP-*HSVtk* and GCV treatment for 5 days resulted in a 50% decrease in tumor volume. Further optimization of AAVP administration (single vs. multiple administrations) and GCV schedules could potentially improve tumor therapy and may aid in the development of clinical translation.

CHAPTER 5: SUMMARY AND SIGNIFICANCE

Targeted delivery of agents from the circulation into intact CNS or into brain tumors thus appears to have great translational relevance. The design and validation of a clinic-ready AAVP-based targeting trans-BBB approach may open the prospect of visualizing the presence of brain tumors and precise determination of location for diagnosis. This could empower managing clinicians to serially quantify spatial changes in response to therapy in real-time. Moreover, one might predict that either genetic disorders globally affecting the CNS (i.e., lysosomal storage and myelin diseases) or degenerative diseases targeted to specific neuronal populations would likely benefit from the attributes of the CRTIGPSVC peptide which, in principle, allows selective delivery of the agents without simultaneous opening of the BBB to potentially harmful blood-derived molecules. The very property of selective opening of the BBB precludes assaying the efficiency of targeted AAVP delivery by the standard methods of measuring transfer of tracers from the blood into CNS parenchyma. Finally, given our human TMA results, the translation of the functional features of peptide-directed particles from animal models into clinical applications may hold promise for the targeted molecular imaging and therapy of brain tumors in cancer patients. Further medical applications against other neurological disorders, especially those with high TfR concentrations may also be envisioned.

CHAPTER 6: REFERENCES

1. CBTRUS. 2008. Statistical report: primary brain tumors in the United States, 1998-2002. Central Brain Tumor Registry of the United States, 2000-2004.
2. Fisher, J. L., J. A. Schwartzbaum, M. Wrensch, and J. L. Wiemels. 2007. Epidemiology of brain tumors. *Neurol Clin* 25:867-890, vii.
3. Furnari, F. B., T. Fenton, R. M. Bachoo, A. Mukasa, J. M. Stommel, A. Stegh, W. C. Hahn, K. L. Ligon, D. N. Louis, C. Brennan, L. Chin, R. A. DePinho, and W. K. Cavenee. 2007. Malignant astrocytic glioma: genetics, biology, and paths to treatment. *Genes Dev* 21:2683-2710.
4. Kleihues, P., D. N. Louis, B. W. Scheithauer, L. B. Rorke, G. Reifenberger, P. C. Burger, and W. K. Cavenee. 2002. The WHO classification of tumors of the nervous system. *J Neuropathol Exp Neurol* 61:215-225; discussion 226-219.
5. Louis, D. N., H. Ohgaki, O. D. Wiestler, W. K. Cavenee, P. C. Burger, A. Jouvet, B. W. Scheithauer, and P. Kleihues. 2007. The 2007 WHO classification of tumours of the central nervous system. *Acta Neuropathol* 114:97-109.
6. Wen, P. Y., and S. Kesari. 2008. Malignant gliomas in adults. *N Engl J Med* 359:492-507.
7. Scherer, H. J. 1940. Cerebral astrocytomas and their derivatives. *Am J Cancer* 40:159-198.
8. Parsons, D. W., S. Jones, X. Zhang, J. C. Lin, R. J. Leary, P. Angenendt, P. Mankoo, H. Carter, I. M. Siu, G. L. Gallia, A. Olivi, R. McLendon, B. A. Rasheed, S. Keir, T. Nikolskaya, Y. Nikolsky, D. A. Busam, H. Tekleab, L. A. Diaz, Jr., J. Hartigan, D. R. Smith, R. L. Strausberg, S. K. Marie, S. M. Shinjo, H. Yan, G. J. Riggins, D. D.

- Bigner, R. Karchin, N. Papadopoulos, G. Parmigiani, B. Vogelstein, V. E. Velculescu, and K. W. Kinzler. 2008. An integrated genomic analysis of human glioblastoma multiforme. *Science* 321:1807-1812.
9. Phillips, H. S., S. Kharbanda, R. Chen, W. F. Forrest, R. H. Soriano, T. D. Wu, A. Misra, J. M. Nigro, H. Colman, L. Soroceanu, P. M. Williams, Z. Modrusan, B. G. Feuerstein, and K. Aldape. 2006. Molecular subclasses of high-grade glioma predict prognosis, delineate a pattern of disease progression, and resemble stages in neurogenesis. *Cancer Cell* 9:157-173.
 10. Sathornsumetee, S., D. A. Reardon, A. Desjardins, J. A. Quinn, J. J. Vredenburgh, and J. N. Rich. 2007. Molecularly targeted therapy for malignant glioma. *Cancer* 110:13-24.
 11. Sathornsumetee, S., J. N. Rich, and D. A. Reardon. 2007. Diagnosis and treatment of high-grade astrocytoma. *Neurol Clin* 25:1111-1139, x.
 12. Stupp, R., W. P. Mason, M. J. van den Bent, M. Weller, B. Fisher, M. J. Taphoorn, K. Belanger, A. A. Brandes, C. Marosi, U. Bogdahn, J. Curschmann, R. C. Janzer, S. K. Ludwin, T. Gorlia, A. Allgeier, D. Lacombe, J. G. Cairncross, E. Eisenhauer, and R. O. Mirimanoff. 2005. Radiotherapy plus concomitant and adjuvant temozolomide for glioblastoma. *N Engl J Med* 352:987-996.
 13. Chi, A. S., and P. Y. Wen. 2007. Inhibiting kinases in malignant gliomas. *Expert Opin Ther Targets* 11:473-496.
 14. Banks, W. A. 2008. Developing drugs that can cross the blood-brain barrier: applications to Alzheimer's disease. *BMC Neurosci* 9 Suppl 3:S2.
 15. Pardridge, W. M. 2007. Blood-brain barrier delivery. *Drug Discov Today* 12:54-61.

16. Ehrlich, P. 1904. Über die Beziehung chemischer Constitution, Vertheilung, und pharmakologischer Wirkung. In Gesammelte Arbeiten zur Immunitätsforschung, Berlin.
17. Goldmann, E. E. 1913. Vitalfärbung am Zentralnervensystem. Abh Preuss Wissensch Phys Math 1:1-60.
18. Abbott, N. J., L. Ronnback, and E. Hansson. 2006. Astrocyte-endothelial interactions at the blood-brain barrier. *Nat Rev Neurosci* 7:41-53.
19. Neuwelt, E., N. J. Abbott, L. Abrey, W. A. Banks, B. Blakley, T. Davis, B. Engelhardt, P. Grammas, M. Nedergaard, J. Nutt, W. Pardridge, G. A. Rosenberg, Q. Smith, and L. R. Drewes. 2008. Strategies to advance translational research into brain barriers. *Lancet Neurol* 7:84-96.
20. Pardridge, W. M. 2002. Drug and gene delivery to the brain: the vascular route. *Neuron* 36:555-558.
21. Zlokovic, B. V. 2008. The blood-brain barrier in health and chronic neurodegenerative disorders. *Neuron* 57:178-201.
22. Leonhardt, H. 1980. Ependym und circumventriculäre Organe. Springer, Berlin Heidelberg, New York.
23. Bär, T. 1980. The vascular system of the cerebral cortex. *Adv Anat Embryol Cell Biol* 59:I-VI,1-62.
24. Gale, N. W., and G. D. Yancopoulos. 1999. Growth factors acting via endothelial cell-specific receptor tyrosine kinases: VEGFs, angiopoietins, and ephrins in vascular development. *Genes Dev* 13:1055-1066.

25. Stewart, P. A., and E. M. Hayakawa. 1987. Interendothelial junctional changes underlie the developmental 'tightening' of the blood-brain barrier. *Brain Res* 429:271-281.
26. Engelhardt, B. 2003. Development of the blood-brain barrier. *Cell Tissue Res* 314:119-129.
27. Robertson, P. L., M. Du Bois, P. D. Bowman, and G. W. Goldstein. 1985. Angiogenesis in developing rat brain: an in vivo and in vitro study. *Brain Res* 355:219-223.
28. Janzer, R. C., and M. C. Raff. 1987. Astrocytes induce blood-brain barrier properties in endothelial cells. *Nature* 325:253-257.
29. Lindahl, P., B. R. Johansson, P. Leveen, and C. Betsholtz. 1997. Pericyte loss and microaneurysm formation in PDGF-B-deficient mice. *Science* 277:242-245.
30. Peppiatt, C. M., C. Howarth, P. Mobbs, and D. Attwell. 2006. Bidirectional control of CNS capillary diameter by pericytes. *Nature* 443:700-704.
31. Suri, C., P. F. Jones, S. Patan, S. Bartunkova, P. C. Maisonpierre, S. Davis, T. N. Sato, and G. D. Yancopoulos. 1996. Requisite role of angiopoietin-1, a ligand for the TIE2 receptor, during embryonic angiogenesis. *Cell* 87:1171-1180.
32. Pardridge, W. M. 2005. The blood-brain barrier: bottleneck in brain drug development. *NeuroRx* 2:3-14.
33. Simpson, I. A., A. Carruthers, and S. J. Vannucci. 2007. Supply and demand in cerebral energy metabolism: the role of nutrient transporters. *J Cereb Blood Flow Metab* 27:1766-1791.

34. Zlokovic, B. V., D. J. Begley, and D. G. Chain-Eliash. 1985. Blood-brain barrier permeability to leucine-enkephalin, D-alanine²-D-leucine⁵-enkephalin and their N-terminal amino acid (tyrosine). *Brain Res* 336:125-132.
35. Vorbrodt, A. W. 1988. Ultrastructural cytochemistry of blood-brain barrier endothelia. *Prog Histochem Cytochem* 18:1-99.
36. Argaw, A. T., B. T. Gurfein, Y. Zhang, A. Zameer, and G. R. John. 2009. VEGF-mediated disruption of endothelial CLN-5 promotes blood-brain barrier breakdown. *Proc Natl Acad Sci U S A* 106:1977-1982.
37. Richardson, D. R., and P. Ponka. 1997. The molecular mechanisms of the metabolism and transport of iron in normal and neoplastic cells. *Biochim Biophys Acta* 1331:1-40.
38. Aisen, P., and I. Listowsky. 1980. Iron transport and storage proteins. *Annu Rev Biochem* 49:357-393.
39. Beutler, E., T. Gelbart, P. Lee, R. Trevino, M. A. Fernandez, and V. F. Fairbanks. 2000. Molecular characterization of a case of atransferrinemia. *Blood* 96:4071-4074.
40. Gomme, P. T., K. B. McCann, and J. Bertolini. 2005. Transferrin: structure, function and potential therapeutic actions. *Drug Discov Today* 10:267-273.
41. Young, S. P., A. Bomford, and R. Williams. 1984. The effect of the iron saturation of transferrin on its binding and uptake by rabbit reticulocytes. *Biochem J* 219:505-510.
42. Harford, J. B., T. H. Rouault, H. A. Huebers, and R. D. Klausner. 1994. Molecular mechanisms of iron metabolism. W.B. Saunders Co., Philadelphia.

43. Cheng, Y., O. Zak, P. Aisen, S. C. Harrison, and T. Walz. 2004. Structure of the human transferrin receptor-transferrin complex. *Cell* 116:565-576.
44. Daniels, T. R., T. Delgado, G. Helguera, and M. L. Penichet. 2006. The transferrin receptor part II: targeted delivery of therapeutic agents into cancer cells. *Clin Immunol* 121:159-176.
45. Daniels, T. R., T. Delgado, J. A. Rodriguez, G. Helguera, and M. L. Penichet. 2006. The transferrin receptor part I: Biology and targeting with cytotoxic antibodies for the treatment of cancer. *Clin Immunol* 121:144-158.
46. Recht, L., C. O. Torres, T. W. Smith, V. Raso, and T. W. Griffin. 1990. Transferrin receptor in normal and neoplastic brain tissue: implications for brain-tumor immunotherapy. *J Neurosurg* 72:941-945.
47. Trowbridge, I. S., and D. L. Domingo. 1981. Anti-transferrin receptor monoclonal antibody and toxin-antibody conjugates affect growth of human tumour cells. *Nature* 294:171-173.
48. Pantopoulos, K. 2004. Iron metabolism and the IRE/IRP regulatory system: an update. *Ann N Y Acad Sci* 1012:1-13.
49. Kawabata, H., R. Yang, T. Hirama, P. T. Vuong, S. Kawano, A. F. Gombart, and H. P. Koeffler. 1999. Molecular cloning of transferrin receptor 2. A new member of the transferrin receptor-like family. *J Biol Chem* 274:20826-20832.
50. Kawabata, H., T. Nakamaki, P. Ikonomi, R. D. Smith, R. S. Germain, and H. P. Koeffler. 2001. Expression of transferrin receptor 2 in normal and neoplastic hematopoietic cells. *Blood* 98:2714-2719.

51. Smith, G. P. 1985. Filamentous fusion phage: novel expression vectors that display cloned antigens on the virion surface. *Science* 228:1315-1317.
52. Ozawa, M. G., F. I. Staquicini, R. L. Sidman, R. Pasqualini, and W. Arap. 2009. Vascular targeting of brain tumors-Bridging the gap with phage display. In *CNS Cancer: Models, Markers, Prognostic factors, and Therapeutic approaches*. E. G. Van Meir, editor. Humana Press, New York.
53. Parmley, S. F., and G. P. Smith. 1988. Antibody-selectable filamentous fd phage vectors: affinity purification of target genes. *Gene* 73:305-318.
54. Scott, J. K., and G. P. Smith. 1990. Searching for peptide ligands with an epitope library. *Science* 249:386-390.
55. Mintz, P. J., J. Kim, K. A. Do, X. Wang, R. G. Zinner, M. Cristofanilli, M. A. Arap, W. K. Hong, P. Troncoso, C. J. Logothetis, R. Pasqualini, and W. Arap. 2003. Fingerprinting the circulating repertoire of antibodies from cancer patients. *Nat Biotechnol* 21:57-63.
56. Vidal, C. I., P. J. Mintz, K. Lu, L. M. Ellis, L. Manenti, R. Giavazzi, D. M. Gershenson, R. Broaddus, J. Liu, W. Arap, and R. Pasqualini. 2004. An HSP90-mimic peptide revealed by fingerprinting the pool of antibodies from ovarian cancer patients. *Oncogene* 23:8859-8867.
57. Barbu, E. M., V. K. Ganesh, S. Gurusiddappa, R. C. Mackenzie, T. J. Foster, T. C. Sudhof, and M. Hook. 2010. beta-Neurexin is a ligand for the *Staphylococcus aureus* MSCRAMM SdrC. *PLoS Pathog* 6:e1000726.

58. Serasinghe, M. N., A. M. Seneviratne, A. V. Smrcka, and Y. Yoon. 2010. Identification and characterization of unique proline-rich peptides binding to the mitochondrial fission protein hFis1. *J Biol Chem* 285:620-630.
59. Wu, P., J. Weisell, M. Pakkala, M. Perakyla, L. Zhu, R. Koistinen, E. Koivunen, U. H. Stenman, A. Narvanen, and H. Koistinen. 2010. Identification of novel peptide inhibitors for human trypsins. *Biol Chem* 391:283-293.
60. Cardó-Vila, M., R. J. Giordano, R. L. Sidman, L. F. Bronk, Z. Fan, J. Mendelsohn, W. Arap, and R. Pasqualini. 2010. From combinatorial peptide selection to drug prototype (II): Targeting the epidermal growth factor receptor pathway. *Proc Natl Acad Sci U S A*.
61. Giordano, R. J., M. Cardó-Vila, J. Lahdenranta, R. Pasqualini, and W. Arap. 2001. Biopanning and rapid analysis of selective interactive ligands. *Nat Med* 7:1249-1253.
62. Kolonin, M. G., L. Bover, J. Sun, A. J. Zurita, K. A. Do, J. Lahdenranta, M. Cardó-Vila, R. J. Giordano, D. E. Jaalouk, M. G. Ozawa, C. A. Moya, G. R. Souza, F. I. Staquicini, A. Kunyiasu, D. A. Scudiero, S. L. Holbeck, E. A. Sausville, W. Arap, and R. Pasqualini. 2006. Ligand-directed surface profiling of human cancer cells with combinatorial peptide libraries. *Cancer Res* 66:34-40.
63. Nishimura, S., S. Takahashi, H. Kamikatahira, Y. Kuroki, D. E. Jaalouk, S. O'Brien, E. Koivunen, W. Arap, R. Pasqualini, H. Nakayama, and A. Kuniyasu. 2008. Combinatorial targeting of the macropinocytotic pathway in leukemia and lymphoma cells. *J Biol Chem* 283:11752-11762.

64. Giordano, R. J., C. D. Anobom, M. Cardo-Vila, J. Kalil, A. P. Valente, R. Pasqualini, F. C. Almeida, and W. Arap. 2005. Structural basis for the interaction of a vascular endothelial growth factor mimic peptide motif and its corresponding receptors. *Chem Biol* 12:1075-1083.
65. Giordano, R. J., M. Cardó-Vila, A. Salameh, C. D. Anobom, B. D. Zeitlin, D. H. Hawke, A. P. Valente, F. C. Almeida, J. E. Nor, R. L. Sidman, R. Pasqualini, and W. Arap. 2010. From combinatorial peptide selection to drug prototype (I): Targeting the vascular endothelial growth factor receptor pathway. *Proc Natl Acad Sci U S A*.
66. Pasqualini, R., and E. Ruoslahti. 1996. Organ targeting in vivo using phage display peptide libraries. *Nature* 380:364-366.
67. Arap, W., R. Pasqualini, and E. Ruoslahti. 1998. Cancer treatment by targeted drug delivery to tumor vasculature in a mouse model. *Science* 279:377-380.
68. Arap, W., M. G. Kolonin, M. Trepel, J. Lahdenranta, M. Cardo-Vila, R. J. Giordano, P. J. Mintz, P. U. Ardel, V. J. Yao, C. I. Vidal, L. Chen, A. Flamm, H. Valtanen, L. M. Weavind, M. E. Hicks, R. E. Pollock, G. H. Botz, C. D. Bucana, E. Koivunen, D. Cahill, P. Troncoso, K. A. Baggerly, R. D. Pentz, K. A. Do, C. J. Logothetis, and R. Pasqualini. 2002. Steps toward mapping the human vasculature by phage display. *Nat Med* 8:121-127.
69. Pentz, R. D., C. B. Cohen, M. Wicclair, M. A. DeVita, A. L. Flamm, S. J. Youngner, A. B. Hamric, M. S. McCabe, J. J. Glover, W. J. Kittiko, K. Kinlaw, J. Keller, A. Asch, J. J. Kavanagh, and W. Arap. 2005. Ethics guidelines for research with the recently dead. *Nat Med* 11:1145-1149.

70. Cardó-Vila, M., A. J. Zurita, R. J. Giordano, J. Sun, R. Rangel, L. Guzman-Rojas, C. D. Anobom, A. P. Valente, F. C. Almeida, J. Lahdenranta, M. G. Kolonin, W. Arap, and R. Pasqualini. 2008. A ligand peptide motif selected from a cancer patient is a receptor-interacting site within human interleukin-11. *PLoS One* 3:e3452.
71. Zurita, A. J., P. Troncoso, M. Cardo-Vila, C. J. Logothetis, R. Pasqualini, and W. Arap. 2004. Combinatorial screenings in patients: the interleukin-11 receptor alpha as a candidate target in the progression of human prostate cancer. *Cancer Res* 64:435-439.
72. Krag, D. N., G. S. Shukla, G. P. Shen, S. Pero, T. Ashikaga, S. Fuller, D. L. Weaver, S. Burdette-Radoux, and C. Thomas. 2006. Selection of tumor-binding ligands in cancer patients with phage display libraries. *Cancer Res* 66:7724-7733.
73. Yong, R. L., N. Shinojima, J. Fueyo, J. Gumin, G. G. Vecil, F. C. Marini, O. Bogler, M. Andreeff, and F. F. Lang. 2009. Human bone marrow-derived mesenchymal stem cells for intravascular delivery of oncolytic adenovirus Delta24-RGD to human gliomas. *Cancer Res* 69:8932-8940.
74. Driessen, W. H., M. G. Ozawa, W. Arap, and R. Pasqualini. 2009. Ligand-directed cancer gene therapy to angiogenic vasculature. *Adv Genet* 67:103-121.
75. Kootstra, N. A., and I. M. Verma. 2003. Gene therapy with viral vectors. *Annu Rev Pharmacol Toxicol* 43:413-439.
76. Mizuguchi, H., and T. Hayakawa. 2004. Targeted adenovirus vectors. *Hum Gene Ther* 15:1034-1044.
77. Hajitou, A., M. Trepel, C. E. Lilley, S. Soghomonyan, M. M. Alauddin, F. C. Marini, 3rd, B. H. Restel, M. G. Ozawa, C. A. Moya, R. Rangel, Y. Sun, K. Zaoui, M.

- Schmidt, C. von Kalle, M. D. Weitzman, J. G. Gelovani, R. Pasqualini, and W. Arap. 2006. A hybrid vector for ligand-directed tumor targeting and molecular imaging. *Cell* 125:385-398.
78. Hajitou, A., R. Rangel, M. Trepel, S. Sghomonyan, J. G. Gelovani, M. M. Alauddin, R. Pasqualini, and W. Arap. 2007. Design and construction of targeted AAVP vectors for mammalian cell transduction. *Nat Protoc* 2:523-531.
 79. Sghomonyan, S., A. Hajitou, R. Rangel, M. Trepel, R. Pasqualini, W. Arap, J. G. Gelovani, and M. M. Alauddin. 2007. Molecular PET imaging of HSV1-tk reporter gene expression using [¹⁸F]FEAU. *Nat Protoc* 2:416-423.
 80. Tjuvajev, J. G., N. Avril, T. Oku, T. Sasajima, T. Miyagawa, R. Joshi, M. Safer, B. Beattie, G. DiResta, F. Daghighian, F. Augensen, J. Koutcher, J. Zweit, J. Humm, S. M. Larson, R. Finn, and R. Blasberg. 1998. Imaging herpes virus thymidine kinase gene transfer and expression by positron emission tomography. *Cancer Res* 58:4333-4341.
 81. Trepel, M., C. A. Stoneham, H. Eleftherohorinou, N. D. Mazarakis, R. Pasqualini, W. Arap, and A. Hajitou. 2009. A heterotypic bystander effect for tumor cell killing after adeno-associated virus/phage-mediated, vascular-targeted suicide gene transfer. *Mol Cancer Ther* 8:2383-2391.
 82. Tandle, A., E. Hanna, D. Lorang, A. Hajitou, C. A. Moya, R. Pasqualini, W. Arap, A. Adem, E. Starker, S. Hewitt, and S. K. Libutti. 2009. Tumor vasculature-targeted delivery of tumor necrosis factor-alpha. *Cancer* 115:128-139.
 83. Paoloni, M. C., A. Tandle, C. Mazcko, E. Hanna, S. Kachala, A. Leblanc, S. Newman, D. Vail, C. Henry, D. Thamm, K. Sorenmo, A. Hajitou, R. Pasqualini, W.

- Arap, C. Khanna, and S. K. Libutti. 2009. Launching a novel preclinical infrastructure: comparative oncology trials consortium directed therapeutic targeting of TNF α to cancer vasculature. *PLoS One* 4:e4972.
84. Shapiro, W. R., G. A. Basler, N. L. Chernik, and J. B. Posner. 1979. Human brain tumor transplantation into nude mice. *J Natl Cancer Inst* 62:447-453.
 85. Moore, A., J. P. Basilion, E. A. Chiocca, and R. Weissleder. 1998. Measuring transferrin receptor gene expression by NMR imaging. *Biochim Biophys Acta* 1402:239-249.
 86. Lal, S., M. Lacroix, P. Tofilon, G. N. Fuller, R. Sawaya, and F. F. Lang. 2000. An implantable guide-screw system for brain tumor studies in small animals. *J Neurosurg* 92:326-333.
 87. Christianson, D. R., M. G. Ozawa, R. Pasqualini, and W. Arap. 2007. Techniques to decipher molecular diversity by phage display. *Methods Mol Biol* 357:385-406.
 88. Kolonin, M. G., P. K. Saha, L. Chan, R. Pasqualini, and W. Arap. 2004. Reversal of obesity by targeted ablation of adipose tissue. *Nat Med* 10:625-632.
 89. Marchiò, S., J. Lahdenranta, R. O. Schlingemann, D. Valdembri, P. Wesseling, M. A. Arap, A. Hajitou, M. G. Ozawa, M. Trepel, R. J. Giordano, D. M. Nanus, H. B. Dijkman, E. Oosterwijk, R. L. Sidman, M. D. Cooper, F. Bussolino, R. Pasqualini, and W. Arap. 2004. Aminopeptidase A is a functional target in angiogenic blood vessels. *Cancer Cell* 5:151-162.
 90. Pasqualini, R., W. Arap, D. Rajotte, and E. Ruoslahti. 2001. In vivo phage display techniques. In *Phage Display, A Laboratory Manual*. C. F. Barbas, III, D. R. Burton,

J. K. Scott, and G. J. Silverman, editors. Cold Spring Harbor Laboratory Press, Woodbury, NY.

91. Mandava, S., L. Makowski, S. Devarapalli, J. Uzubell, and D. J. Rodi. 2004. RELIC-
-a bioinformatics server for combinatorial peptide analysis and identification of
protein-ligand interaction sites. *Proteomics* 4:1439-1460.
92. Altschul, S. F., W. Gish, W. Miller, E. W. Myers, and D. J. Lipman. 1990. Basic
local alignment search tool. *J Mol Biol* 215:403-410.
93. Dias-Neto, E., D. N. Nunes, R. J. Giordano, J. Sun, G. H. Botz, K. Yang, J. C.
Setubal, R. Pasqualini, and W. Arap. 2009. Next-generation phage display:
integrating and comparing available molecular tools to enable cost-effective high-
throughput analysis. *PLoS One* 4:e8338.
94. Boado, R. J., and M. M. Pardridge. 1991. A one-step procedure for isolation of
poly(A)⁺ mRNA from isolated brain capillaries and endothelial cells in culture. *J*
Neurochem 57:2136-2139.
95. Triguero, D., J. Buciak, and W. M. Pardridge. 1990. Capillary depletion method for
quantification of blood-brain barrier transport of circulating peptides and plasma
proteins. *J Neurochem* 54:1882-1888.
96. Wang, H., W. Zhang, and G. N. Fuller. 2006. Overexpression of IGFBP5, but not
IGFBP3, correlates with the histologic grade of human diffuse glioma: a tissue
microarray and immunohistochemical study. *Technol Cancer Res Treat* 5:195-199.
97. Alauddin, M. M., and P. S. Conti. 1998. Synthesis and preliminary evaluation of 9-
(4-[¹⁸F]-fluoro-3-hydroxymethylbutyl)guanine ([¹⁸F]FHBG): a new potential

- imaging agent for viral infection and gene therapy using PET. *Nucl Med Biol* 25:175-180.
98. Alauddin, M. M., A. Y. Louie, A. Shahinian, T. J. Meade, and P. S. Conti. 2003. Receptor mediated uptake of a radiolabeled contrast agent sensitive to beta-galactosidase activity. *Nucl Med Biol* 30:261-265.
 99. Cardó-Vila, M., W. Arap, and R. Pasqualini. 2003. Alpha v beta 5 integrin-dependent programmed cell death triggered by a peptide mimic of annexin V. *Mol Cell* 11:1151-1162.
 100. MacGillivray, R. T., S. A. Moore, J. Chen, B. F. Anderson, H. Baker, Y. Luo, M. Bewley, C. A. Smith, M. E. Murphy, Y. Wang, A. B. Mason, R. C. Woodworth, G. D. Brayer, and E. N. Baker. 1998. Two high-resolution crystal structures of the recombinant N-lobe of human transferrin reveal a structural change implicated in iron release. *Biochemistry* 37:7919-7928.
 101. Friden, P. M., L. R. Walus, G. F. Musso, M. A. Taylor, B. Malfroy, and R. M. Starzyk. 1991. Anti-transferrin receptor antibody and antibody-drug conjugates cross the blood-brain barrier. *Proc Natl Acad Sci U S A* 88:4771-4775.
 102. Dayani, P. N., M. C. Bishop, K. Black, and P. M. Zeltzer. 2004. Desferoxamine (DFO)--mediated iron chelation: rationale for a novel approach to therapy for brain cancer. *J Neurooncol* 67:367-377.
 103. Mason, A. B., Q. Y. He, T. E. Adams, D. R. Gumerov, I. A. Kaltashov, V. Nguyen, and R. T. MacGillivray. 2001. Expression, purification, and characterization of recombinant nonglycosylated human serum transferrin containing a C-terminal hexahistidine tag. *Protein Expr Purif* 23:142-150.

104. James, N. G., C. L. Berger, S. L. Byrne, V. C. Smith, R. T. MacGillivray, and A. B. Mason. 2007. Intrinsic fluorescence reports a global conformational change in the N-lobe of human serum transferrin following iron release. *Biochemistry* 46:10603-10611.
105. James, N. G., S. L. Byrne, A. N. Steere, V. C. Smith, R. T. MacGillivray, and A. B. Mason. 2009. Inequivalent contribution of the five tryptophan residues in the C-lobe of human serum transferrin to the fluorescence increase when iron is released. *Biochemistry* 48:2858-2867.
106. Byrne, S. L., and A. B. Mason. 2009. Human serum transferrin: a tale of two lobes. Urea gel and steady state fluorescence analysis of recombinant transferrins as a function of pH, time, and the soluble portion of the transferrin receptor. *J Biol Inorg Chem* 14:771-781.
107. Shen, Z. M., J. T. Yang, Y. M. Feng, and C. S. Wu. 1992. Conformational stability of porcine serum transferrin. *Protein Sci* 1:1477-1484.
108. Jeffrey, P. D., M. C. Bewley, R. T. MacGillivray, A. B. Mason, R. C. Woodworth, and E. N. Baker. 1998. Ligand-induced conformational change in transferrins: crystal structure of the open form of the N-terminal half-molecule of human transferrin. *Biochemistry* 37:13978-13986.
109. Thakurta, P. G., D. Choudhury, R. Dasgupta, and J. K. Dattagupta. 2004. Tertiary structural changes associated with iron binding and release in hen serum transferrin: a crystallographic and spectroscopic study. *Biochem Biophys Res Commun* 316:1124-1131.

110. Prior, R., G. Reifenberger, and W. Wechsler. 1990. Transferrin receptor expression in tumours of the human nervous system: relation to tumour type, grading and tumour growth fraction. *Virchows Arch A Pathol Anat Histopathol* 416:491-496.
111. Geier, M. R., M. E. Trigg, and C. R. Merrill. 1973. Fate of bacteriophage lambda in non-immune germ-free mice. *Nature* 246:221-223.
112. Ozawa, M. G., A. J. Zurita, E. Dias-Neto, D. N. Nunes, R. L. Sidman, J. G. Gelovani, W. Arap, and R. Pasqualini. 2008. Beyond receptor expression levels: the relevance of target accessibility in ligand-directed pharmacodelivery systems. *Trends Cardiovasc Med* 18:126-132.
113. Kemper, E. M., W. Leenders, B. Kusters, S. Lyons, T. Buckle, A. Heerschap, W. Boogerd, J. H. Beijnen, and O. van Tellingen. 2006. Development of luciferase tagged brain tumour models in mice for chemotherapy intervention studies. *Eur J Cancer* 42:3294-3303.
114. Hajitou, A., D. C. Lev, J. A. Hannay, B. Korchin, F. I. Staquicini, S. Soghomonyan, M. M. Alauddin, R. S. Benjamin, R. E. Pollock, J. G. Gelovani, R. Pasqualini, and W. Arap. 2008. A preclinical model for predicting drug response in soft-tissue sarcoma with targeted AAVP molecular imaging. *Proc Natl Acad Sci U S A* 105:4471-4476.
115. Network, T. C. G. A. R. 2008. Comprehensive genomic characterization defines human glioblastoma genes core pathways. *Nature* 455:1061-1068.
116. Sergeeva, A., M. G. Kolonin, J. J. Molldrem, R. Pasqualini, and W. Arap. 2006. Display technologies: application for the discovery of drug and gene delivery agents. *Adv Drug Deliv Rev* 58:1622-1654.

117. Byrne, S. L., N. D. Chasteen, A. N. Steere, and A. B. Mason. 2010. The unique kinetics of iron release from transferrin: the role of receptor, lobe-lobe interactions, and salt at endosomal pH. *J Mol Biol* 396:130-140.

CHAPTER 7: VITA

Michael Gentoshi Ozawa was born in Hayward, California on January 3, 1979. He graduated in the top 5% of seniors from Los Gatos High School, and matriculated to the University of California, San Diego in the fall of 1997. He completed a Bachelor of Science degree in Biochemistry and Cell Biology with a minor in Economics. He subsequently accepted a position as a Postgraduate Researcher at the University of California, San Francisco in the laboratory of Dr. Donald M. McDonald, studying angiogenesis in chronic inflammation and cancer. In 2003, he joined the laboratory of Drs. Wadih Arap and Renata Pasqualini at the University of Texas M. D. Anderson Cancer Center as a Research Assistant II, continuing studies related to angiogenesis and vascular targeting. He entered the M.D./Ph.D. program at the University of Texas Health Sciences Center in the fall of 2005. Following the completion of his first two years of medical training, he selected to pursue his graduate studies under the mentorship of Dr. Wadih Arap in 2007, developing novel strategies to deliver agents to the normal brain and brain tumors.

Permanent Address:

3779 Syracuse Street

Houston, TX 77005